

Global Alignment of the CMS Muon System with Tracks using an Extended HIP Algorithm

Jim Pivarski, Alexei Safonov, Karoly Banicz, Riccardo Bellan

May 1, 2009

Abstract

We describe a track-based muon system alignment system using an extended HIP algorithm. We present the details of the procedure and its validation with Monte Carlo simulation studies and discuss data-driven monitoring and verification of alignment results. We applied this procedure to align the muon system with cosmic ray data taken in 2008, and a variant of the procedure with beam-halo muons from the 2008 LHC run, and present the results here.

Contents

1	Introduction	3
1.1	Geometry of the muon system	4
2	Description of the global alignment algorithm	7
2.1	Alignment datasets and track-fitting procedures	8
2.2	Calculation of super-residuals	9
2.3	Differential geometry of super-residuals	11
2.4	Fitting the residuals distribution	13
2.5	Accommodating errors in magnetic field and material budget	18
3	Monitoring Tools and Validation/Verification	21
3.1	Validating residuals fits	22
3.2	Comparison of geometries in the database	23
3.3	Muon system maps	23
3.4	Verification with relative residuals	26
4	Global alignment results with collisions Monte Carlo	29
4.1	Scaling with statistics	29
4.2	Dependence on tracker misalignment	29
4.3	Dependence on magnetic field errors	29
5	Global alignment results with cosmic ray data	29
5.1	Validation plots	29
5.2	Verification with relative residuals	29
5.3	Verification with stand-alone muon alignments	29
5.4	Verification with cosmic track splitting	30
6	Relative alignment of CSCs with local tracks	30
6.1	Description of the CSC Overlaps algorithm	30
6.2	Local CSC alignment parameters	32
6.3	Specialized trigger and data streams	33
6.4	Results from the 2008 LHC run	34
6.5	Extension to align CSC layers	37
6.6	Verifying the global procedure with local alignment	39
7	Alignment outlook for 2009–2010	40

1 Introduction

The CMS experiment features a large muon tracking system which will be essential for early LHC discoveries. As with all tracking systems, the resolution of its reconstructed tracks depends on two main components:

- intrinsic hit resolution, or how precisely the intersection of passing particles with its measurement planes can be determined for individual tracks, and
- alignment, or how accurately the position of the measurement planes are known in 3-D space, affecting all tracks.

These components combine in quadrature, so track resolution can be expected to improve significantly until the alignment is much better than the intrinsic resolution, which is about 200–300 μm for the CMS muon system. Therefore, our baseline goal for the 2009–2010 physics run is to align the muon system to this level of accuracy.

Though this 44-layer muon system can act as a tracking system on its own, it was designed to operate in conjunction with the other CMS subsystems, particularly the inner silicon tracker. Together, the two tracking subsystems form a global tracking system with high intrinsic hit resolution in the tracker and large lever arm in the muon system (particularly important for high- p_T tracks; $1/p_T$ resolution scales with the length of the usable radial lever arm squared). Above $p_T \gtrsim 200$ GeV in the barrel and 1 TeV in the endcap, the inclusion of muon system hits significantly improves muon resolution over a tracker-only measurement (Fig 1). Muon alignment is therefore important for any physics analysis featuring high- p_T muons, such as $Z' \rightarrow \mu\mu$ and $W' \rightarrow \mu\nu$, but it is also important for analyses that use the muon system as an independent check on the tracker, such as the search for heavy stable charged particles, which verifies velocity from tracker dE/dx with muon barrel timing (equivalent to spatial resolution).

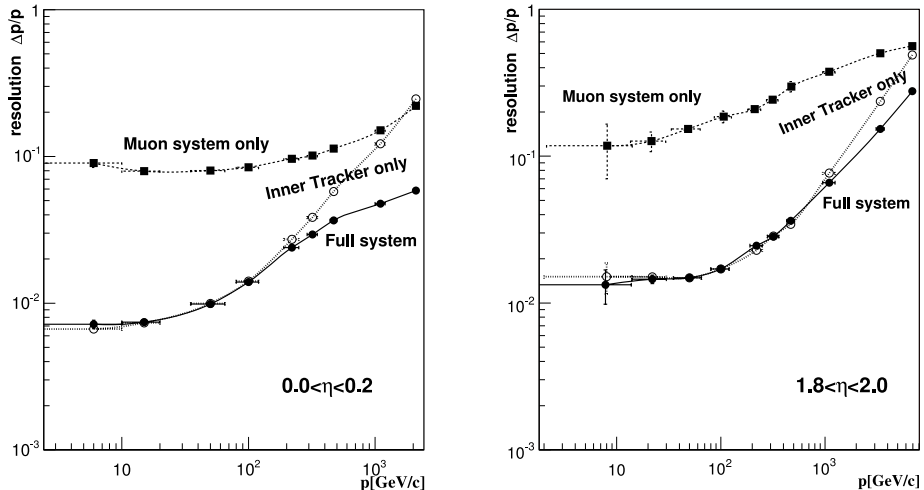


Figure 1: Momentum resolution of the inner tracker, muon system, and combined system, as a function of p_T and η . (Source: Physics TDR [1])

To obtain high-quality global muon tracks, the tracker and muon system must be aligned in the same coordinate system. We choose to define the global coordinate system as the inner tracker’s system and verify that it is stable for each block of runs. This is convenient because the low-momentum tracks used to measure the alignment (20–100 GeV) are best determined by the tracker. If a sudden movement or slow drift is observed, we have the necessary machinery to redefine the global coordinate system in a more neutral way.

There are several independent ways to measure alignment, all of which are actively being pursued. Alignment with global muon tracks provides a simple way to link distant subdetector elements and is sensitive to exactly the same parameters as the muon tracks used in physics analyses. For example, if misalignment perpendicular to the measurement plane of a layer cannot be determined from a large sample of tracks, then it also does not distort the physics resolution of muons in the same sized sample. Alignment with local tracks, such as linear track stubs through pairs of neighboring detector elements, can determine the relative positions of those elements and provide both an early (low statistics) alignment measurement and a powerful cross-check on the global alignment, as local tracks are much less sensitive to propagation errors and have a different pattern of correlations. The CMS muon system is also instrumented with a network of physical measurement devices such as lasers, calipers, and inclinometers, which provide another independent measurement of detector alignment, free from any tracking errors but requiring a careful propagation of cumulative measurements. This paper will focus on alignment with global tracks for both the barrel and the endcap, and demonstrate an alignment procedure with local tracks in the endcap.

1.1 Geometry of the muon system

The muon system contains three basic types of tracking chambers: drift tube (DT) chambers in the barrel, cathode strip chambers (CSC) in the endcap, and resistive plate chambers (RPC) in both. The chambers are modular tracking detectors, 1–4 m each, whose internal geometry is well understood from production tests. They are mounted on 15 m tall barrel wheels and endcap disks which serve to compactly return the solenoid’s magnetic field and also filter all particles except for muons. The position and orientation of each chamber is allowed to slip under the influence of the 3.8 T CMS solenoid, rather than distort the chambers non-rigidly. In the center of the endcap, this distortion can be as large as 1.4 cm.

This paper focuses on algorithms to align the DT chambers and CSCs as rigid bodies whose internal geometry is assumed to be known. The DT internal geometry has been thoroughly studied elsewhere [2], and a method to align CSC layers will be described in section 6.5. The RPCs are used primarily for triggering with a resolution of 1–2 cm, so they do not contribute to muon resolution and do not need to be aligned regularly.

The chambers are grouped in stations (loosely by distance from the interaction point), wheels/disks (modular transverse slices), and sectors/chambers (azimuthal divisions). Table 1 presents an overview of this structure, and Fig 2 shows where the stations are located in CMS.

The CMS global coordinate system is defined with respect to the LHC beamline: the $+z$ direction points along the beamline, to the west. The $+y$ axis is vertically upward, with $+x$ forming a right-handed coordinate system by pointing south, toward the center of the LHC ring. The same coordinates can be expressed cylindrically, with x and y replaced by

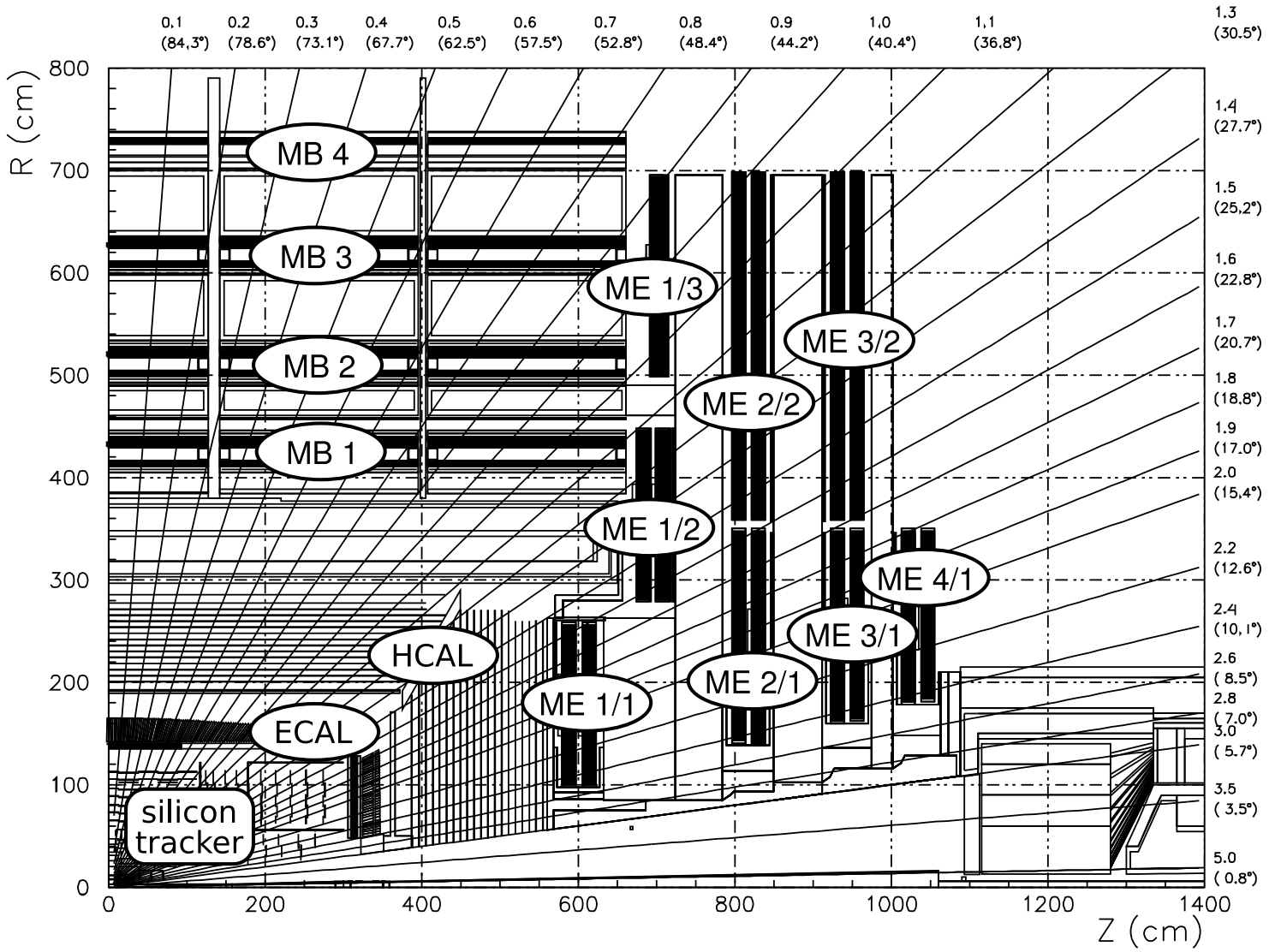


Figure 2: A quarter-view of CMS with labeled muon barrel (MB) and endcap (ME) stations.

Table 1: Geographical organization of muon chambers.

Barrel			Endcap		
wheels	-2 to +2	physically moveable transverse slices	endcaps	- and +	forward and backward halves
stations	MB1 to 4	cylinders of fixed radius from beam-line	disks	ME1 to 4	physically moveable transverse slices
sectors	1-12 (1-14 in station 4)	$\phi = 0$ is sector 1, increasing counter-clockwise	rings (stations)	1/1ab, 1/2, 1/3, 2/1, 2/2, 3/1, 3/2, 4/1	rings of fixed radius from beamline
			chambers	1-36 (1-18 in 2/1, 3/1, 4/1)	$\phi = 0$ is sector 1, increasing counter-clockwise

$r = \sqrt{x^2 + y^2}$ and $\phi = \text{atan2}(y, x)$, which is often more natural given CMS's near-cylindrical symmetry [3]. We use the curvilinear coordinate $r\phi$ to denote a direction perpendicular to z and r , at a given r , in units of length. Differentials of $r\phi$ (e.g. $d(r\phi)/dz$) vary in ϕ , not r (so they are equivalent to $r d\phi/dz$).

Each muon chamber and layer has its own local coordinate system, centered on the subdetector with local z being perpendicular to the measurement plane. The local x direction is always the direction measured with highest precision, roughly corresponding with global $r\phi$, and local y forms a right-handed coordinate system. In barrel stations 1-3, DT chambers measure x and y with different superlayers: superlayers 1 and 3 measure local x coordinates and superlayer 2 (located between 1 and 3) measures local y , roughly parallel with the beamline. In the absence of misalignment, the DT local y axis is exactly parallel with global z . Barrel station 4 chambers have no superlayer 2, so they can not measure y positions of hits.

In the CSCs, cathode strips fan radially from the beamline, intersected by anode wires. The strips measure a coordinate perpendicular to their orientation, differing from global $r\phi$ only due to misalignment. The local cartesian x direction is parallel with the strip measurement in the center of the chamber, and y is roughly radial. In the CSCs, local z is parallel with global z , differing in sign for half of the chambers. Table 2 summarizes all of these coordinate systems.

Layer coordinate systems differ from their parent chamber's in only three ways: they have a different origin, with $z = 0$ being centered on the physical measurement plane, DT superlayer 2 is rotated 90° , and layers may require small alignment corrections. Hit

Table 2: Definitions and correspondance of coordinate systems.

Global frame		Local DT frames		Local CSC frames	
x	horizontal, toward center of LHC	x	superlayer 1 and 3 measurement, roughly global $r\phi$	x	strip measurement, roughly global $r\phi$
y	vertical, up				
z	along beamline	y	superlayer 2 measurement, roughly global z	y	wire measurement, roughly radial from beamline
origin	nominal interaction point				
$r\phi$	combination of x and y perpendicular to rays from the beamline	z	out of plane, roughly radial from beamline	z	out of plane, roughly global z
		origin	center of chamber	origin	center of chamber

ϕ_x , ϕ_y , and ϕ_z are rotation angles around local coordinate axes.

positions are measured in the layer coordinate system, and must be transformed to the chamber system when calculating chamber corrections, particularly angles, since these are defined with respect to the chamber’s center.

2 Description of the global alignment algorithm

The basic idea is to accumulate high- p_T muons which pass through two regions: a well-aligned “Reference” volume, usually the silicon tracker, and the “Target” volume under study. Muon tracks are fitted using information from the Reference only, and alignables in the Target (muon chambers, layers, wheels, or disks) are translated and rotated to minimize the difference between muon hits and the intersection of tracks with the layer planes (residuals).

This procedure can be seen as an extreme limit of the HIP algorithm (“Hits and Impact Points,” where impact points are the track intersections) used to align the silicon tracker [4], in which tracks are fitted in a single tracking volume with large uncertainties in the positions of the alignables. The uncertainties reduce the sensitivity of the final track fits to outlying alignables, so that these alignables will have larger residuals. Those residuals may be biased and not represent the whole misalignment, but repeated applications of the procedure draws alignables closer to their rightful positions and finally converges when a fully consistent system is reached.

In comparison with the silicon tracker case, however, individual tracks propagated through the muon system are much less trustworthy due to the large amounts of material they must penetrate. Muons, particularly low-momentum muons, can be highly deflected by the single and multiple scattering which occurs unpredictably in dense material, and can distort the track-fit if not recognized by the algorithm. CMS’s Kalman track-fitting algorithm properly includes such scattering, but as a by-product, tracks fitted to misaligned chambers can be

misinterpreted as scattering in the iron before entering the chamber. Each Kalman track-fit is performed independently, so the systematic nature of misalignment would be ignored, biasing all tracks in the sample. By instead propagating the tracks from the Reference volume through the Target, not allowing Target hits to refine the propagated track, only the muons that actually do scatter significantly are useless for alignment.

The technique is particularly useful when the Reference volume is the silicon tracker, since the tracker dominates the precision of track parameters for the muons used in alignment ($20 < p_T < 100$ GeV). The disadvantage is that any distortions in the tracker geometry, which can persist after completing tracker alignment if the χ^2 of its tracks are invariant under such transformations, would be extrapolated to the muon system, distorting the muon geometry in the same way. However, the broad track angle distribution of cosmic rays allows us to observe residuals on tracks from different parts of the Reference volume, and therefore put bounds on the bias from the track source. The tracker alignment procedure uses this same technique to constrain its “weak modes,” but the muon system provides additional checks with a longer lever arm, to amplify the errors and more easily notice the effects.

It is also a computationally useful feature that excluding Target hits from the track-fit eliminates the coupling between track-fitting and alignment. We therefore do not need to iterate the procedure, as in the case in the tracker-HIP alignment, because geometry updates in the Target have no effect on track-fitting in the Reference. In the language of MillePede-based algorithms, the matrix of alignment parameters and track parameters becomes block-diagonal, greatly simplifying its inversion and eliminating the fundamental distinction between the HIP and MillePede approaches.

2.1 Alignment datasets and track-fitting procedures

Data used for muon HIP alignment are derived from three main sources: LHC collisions, cosmic rays that pass through the tracker, and cosmic rays that do not pass through the tracker. The main difference between the three datasets is the pattern of chambers and tracker silicon wafers they connect. An alignment procedure may be represented by a graph of Reference and Target detector elements (the vertices of the graph) connected by tracks (the edges). Tracks measure the relative positions of the detector elements they connect, and loops in the graph provide consistency checks to confirm that relative positions are transitive (as they must be if they represent true positions in space). Muons from LHC collisions always pass through nearly the same set of detector elements, so they connect silicon wafers to muon chambers as a directed tree. If the silicon wafers that “point” to a given muon chamber are coherently misaligned, this misalignment would be propagated to the muon chamber.

Cosmic rays do not originate from a point source, so they connect muon chambers to silicon wafers in a more complicated mesh with many loops. Each muon chamber receives cosmic rays from a variety of paths through the tracker, effectively averaging over any residual misalignments in it. The disadvantage of cosmic rays is that their distribution is highly non-uniform, with a hit distribution peaking steeply at the top and bottom of the detector, especially if these cosmic rays are also required to pass through the tracker. Cosmic rays that do not pass through the tracker have a more inclusive distribution, but lack a high-precision Reference. It should also be noted that the number of cosmic ray muons (μ^-) is not equal to the number of cosmic ray antimuons (μ^+), especially in regions of the detector

where one sign of curvature points inward, toward more detector elements, and the other points outward. Some tracking biases affect μ^- tracks differently than μ^+ tracks, a point which we will consider in more detail later.

The production mechanism of our collisions muons does not need to be controlled, only the p_T distribution. Whether a muon was the product of a b decay or a Z decay, its propagation through the tracker and muon system is determined solely by its momentum. We therefore only require one muon in the event, with $20 \text{ GeV} < p_T < 100 \text{ GeV}$. The lower limit excludes tracks that are likely to scatter and the upper limit guarantees that track parameters are well determined by the tracker. The muons selected this way are primarily from heavy flavor sources, and the spectrum is steeply peaked at low momentum.

The events are collected by AlCaReco producers (fully-Reconstructed formats for Alignment and Calibration), which select good muon tracks in prompt reconstruction at CERN’s Tier-0 computing center, reduce the data streams to include only the needed tracks and hits, and send them to the CMS CAF (Computing Analysis Farm) to be persistently stored on a local disk. The AlCaReco stream for collisions muons is named MuAlCallIsolatedMu (though no isolation requirements are applied), the stream for cosmics that pass through the tracker is MuAlGlobalCosmics (because they are combined into global tracks with both tracker and muon hits), and the stream for the rest of the cosmic rays is MuAlStandAloneCosmics (stand-alone tracks are reconstructed in the muon system only).

The first step in the alignment algorithm is to re-fit the tracks, using the original track parameters to seed the new fit. This allows us to take advantage of any updates in the Reference geometry and to include artificially large chamber position uncertainties in the Target hit positions (1000 cm, isotropically in x - y - z). The Target hits are technically included in the track re-fit, but the large uncertainty makes them effectively ignored, with nearly zero pull in the fit. The advantage of this method over simply dropping the Target hits is that residuals are calculated using the same routines as standard track-fitting, inheriting any bug-fixes included in standard tracking. These chamber position uncertainties (called Alignable Position Errors, or APEs) are expressed in a mutable database record, so the boundary between the Reference and Target volumes can be arbitrarily defined.

In performing the track re-fit, it is essential that the algorithm starts with the Reference hits and ends with the target hits; otherwise, the new track’s trajectory through the Target will be determined by the old seed track, rather than a new fit to the Reference. For collisions muons, this means that fitting must be performed in the direction of muon momentum (“alongMomentum” or “insideOut”), and for cosmic rays, two specialized refitters, globalCosmicMuonTrajectories and standAloneMuonTrajectories, have been written to set the hit order in a reliable way. The globalCosmicMuonTrajectories algorithm arranges hits to start in the tracker and end in the muon system, while standAloneMuonTrajectories requires the first hit to be closest to the center of CMS (in global z) and the last to be farthest. Thus Reference volumes in the muon system must always include the central barrel wheel (wheel 0): alignment knowledge is propagated from wheel 0 out to the endcaps.

2.2 Calculation of super-residuals

As a tracking volume, the muon system is highly structured. Inside of each chamber, muons encounter negligible material, and in the barrel chambers, also very little magnetic field.

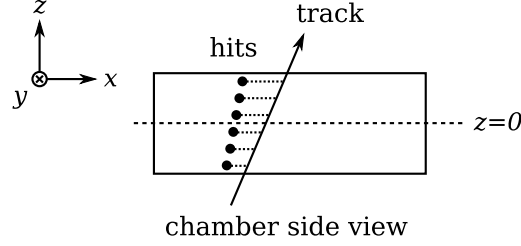


Figure 3: A super-residual has two or four components: the slope of individual x residuals versus the z positions of their layers ($\Delta \frac{dx}{dz}$), their intercept at $z = 0$ (Δx), and the same for y residuals, if measured.

Between chambers, muons pass through thick, magnetized iron and potentially change direction due to scattering. Individual muon hits are therefore more highly correlated with their neighbors in the same chamber than they are with the paths of propagated tracks. We find it useful to combine all residuals in each chamber on each track into a “super-residual” representing the difference in position and angle between the propagated track and all of the hits.

Ignoring the correlation between residuals would lead to an improper treatment of statistics. For the sake of argument, consider an extreme case in which residuals in an N -layer chamber are 100% correlated with each other (no intrinsic error). If we accumulate a histogram of residuals for that chamber, each track will yield the same result N times, though the distribution would be determined by the uncertainties in track propagation. If we then compute the mean of that distribution or fit it, the reported uncertainties would be a factor of \sqrt{N} too small.

A super-residual is an analytic linear fit to all residuals in one chamber on one track (Fig 3). It is expressed in the chamber’s local coordinate system, in which each hit lies on a layer of fixed z_i , with $z = 0$ being the chamber’s center. Denoting the individual residuals as Δx_i and the corresponding hit uncertainties as σ_i , the super-residual position Δx and angle $\Delta \frac{dx}{dz}$ are

$$\Delta x = \frac{1}{\text{denominator}} \left(\sum \frac{z_i^2}{\sigma_i^2} \sum \frac{\Delta x_i}{\sigma_i^2} - \sum \frac{z_i}{\sigma_i^2} \sum \frac{z_i \Delta x_i}{\sigma_i^2} \right) \quad (1)$$

$$\Delta \frac{dx}{dz} = \frac{1}{\text{denominator}} \left(\sum \frac{1}{\sigma_i^2} \sum \frac{z_i \Delta x_i}{\sigma_i^2} - \sum \frac{z_i}{\sigma_i^2} \sum \frac{\Delta x_i}{\sigma_i^2} \right) \quad (2)$$

$$\text{where denominator} = \sum \frac{1}{\sigma_i^2} \sum \frac{z_i^2}{\sigma_i^2} - \left(\sum \frac{z_i}{\sigma_i^2} \right)^2. \quad (3)$$

Chambers that are capable of measuring local y positions of hits have a super-residual Δy and $\Delta \frac{dy}{dz}$ defined the same way.

Note that this differs from simply averaging the residuals, because the fit guarantees that Δx and Δy represent the difference between the track propagation and chamber measurement at the chamber origin ($z = 0$). It also differs from “segment residuals,” in which the raw hit positions are fitted to a straight line instead of hit residuals. A segment residual injects

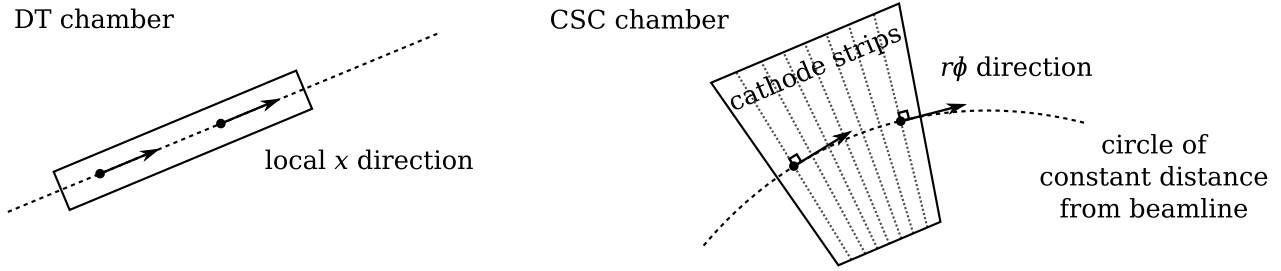


Figure 4: Local x and y coordinates in DT chambers are rectilinear, but the fanning of CSC strips makes it more convenient to measure residuals and align CSCs in curvilinear $r\phi$.

the assumption that tracks propagate linearly through the chamber, while a super-residual only assumes that small errors grow linearly. This is particularly important for chambers immersed in a large magnetic field, such as ME1/1 and ME1/2.

Each super-residual also has a corresponding quality-of-fit parameter

$$\chi^2/\text{ndf} = \frac{1}{N-2} \sum \frac{(x_i - \Delta x - \Delta \frac{dx}{dz} z_i)^2}{\sigma_i^2} \quad (4)$$

which can be used to identify super-residuals containing spurious hits. Rather than applying a cut at an arbitrary χ^2/ndf value, we later use them as weights to prefer straight super-residuals in alignment. Super-residuals are, however, required to contain a hit on every layer in the chamber.

DT super-residuals have four coordinates, Δx , Δy , $\Delta \frac{dx}{dz}$, and $\Delta \frac{dy}{dz}$, except for chambers in station 4. Station 4 chambers have only Δx and $\Delta \frac{dx}{dz}$ because they lack a y -measuring superlayer 2.

CSC super-residuals are computed in a curvilinear coordinate system with two coordinates, $\Delta r\phi$ and $\Delta \frac{d(r\phi)}{dz}$. Angled strips measure residuals perpendicular to the strip angle (Fig 4), a direction which roughly corresponds to global $r\phi$. Local y positions, determined by anode wires, are unreliable because they are ganged in groups as large as 5 cm, much larger than the scale of misalignments. Alignment depends sensitively on the peak of a well-understood residuals distribution, and the discretization in y complicates that shape. The CSC super-residual coordinates are calculated using Eqn 3 with Δx_i replaced by $\Delta r\phi_i$, where the latter is the difference between track and hit in the local direction perpendicular to the strip angle. Alignment in a curvilinear coordinate system has consequences that will be addressed in the next section.

2.3 Differential geometry of super-residuals

Super-residuals (henceforth simply referred to as “residuals”) quantify the misalignment of muon chambers because a small error in the transformation from local hit positions to global hit positions leads to systematic offsets between hits and unbiased tracks. It is useful to separate the geometric contribution, Δx^{geom} , from the measurement error, Δx^{meas} , a random variable centered on zero if there is no bias. The observed residuals distribution is the sum of these two contributions.

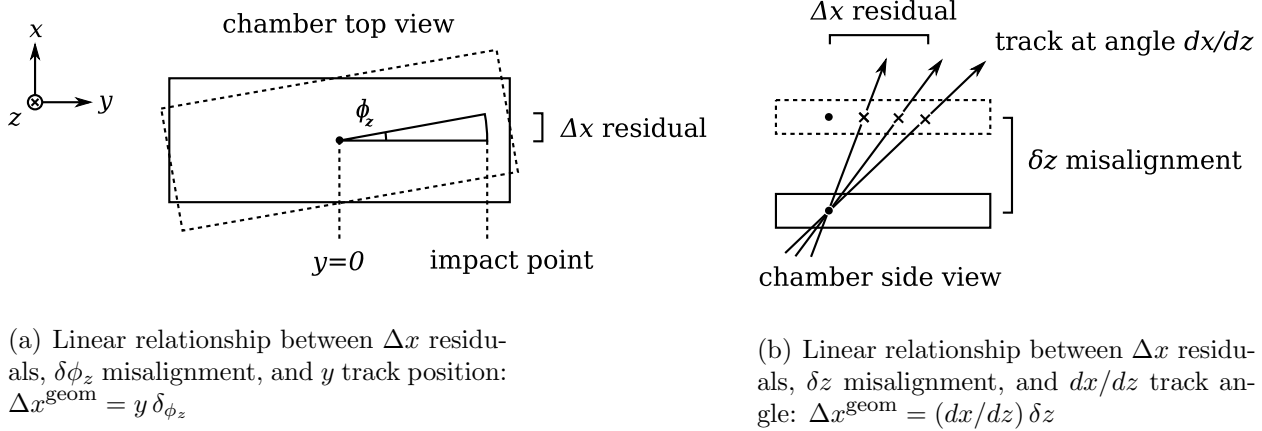


Figure 5: Geometric relationships between δ_z , $\delta\phi_z$ misalignments and Δx residuals.

Geometric residuals are a projection of the misalignment onto Δx^{geom} , Δy^{geom} , $\Delta \frac{dx}{dz}^{\text{geom}}$, and $\Delta \frac{dy}{dz}^{\text{geom}}$. For some misalignments, this projection is trivial: a 1 mm δ_x misalignment (in the chamber's local x direction) does not affect any residuals components except Δx^{geom} , which is shifted by 1 mm. Other misalignments, such as $\delta\phi_z$ and δz introduce Δx^{geom} residuals which depend on the track's intersection point (x, y) and entrance angle $(\frac{dx}{dz}, \frac{dy}{dz})$ on the chamber (Fig 5).

In general, the transformation from rigid body misalignments δ_x , δ_y , δ_z , $\delta\phi_x$, $\delta\phi_y$, and $\delta\phi_z$ to residuals is given by the following transformation:

$$\begin{pmatrix} \Delta x^{\text{geom}} \\ \Delta y^{\text{geom}} \\ \Delta \frac{dx}{dz}^{\text{geom}} \\ \Delta \frac{dy}{dz}^{\text{geom}} \end{pmatrix} = \begin{pmatrix} 1 & 0 & -\frac{dx}{dz} & -y \frac{dx}{dz} & x \frac{dx}{dz} & -y \\ 0 & 1 & -\frac{dy}{dz} & -y \frac{dy}{dz} & x \frac{dy}{dz} & x \\ 0 & 0 & 0 & -\frac{dx}{dz} \frac{dy}{dz} & 1 + \left(\frac{dx}{dz}\right)^2 & -\frac{dy}{dz} \\ 0 & 0 & 0 & -1 - \left(\frac{dy}{dz}\right)^2 & \frac{dx}{dz} \frac{dy}{dz} & \frac{dx}{dz} \end{pmatrix} \begin{pmatrix} \delta_x \\ \delta_y \\ \delta_z \\ \delta\phi_x \\ \delta\phi_y \\ \delta\phi_z \end{pmatrix}. \quad (5)$$

Even without measurement error, the alignment problem cannot be solved with just one track, since the 6 parameters are projected onto fewer residuals components. One needs a collection of tracks sampling different values of $(x, y, \frac{dx}{dz}, \frac{dy}{dz})$ to constrain the problem. (Imagine a $4N \times 6$ matrix constructed from copies of the above for N sets of residuals and track parameters.) The top two rows of this Jacobian are known as Karimaki derivatives, used to align 2-D silicon wafers in the tracker [4]. The additional $\Delta \frac{dx}{dz}^{\text{geom}}$ and $\Delta \frac{dy}{dz}^{\text{geom}}$ angular residuals increase our sensitivity to $\delta\phi_x$ and $\delta\phi_y$, since the matrix elements relating them have magnitudes greater than or equal to 1 for all tracks.

DT chambers in station 4 observe only Δx^{geom} and $\Delta \frac{dx}{dz}^{\text{geom}}$, so their transformation is a

submatrix of the above,

$$\begin{pmatrix} \Delta x^{\text{geom}} \\ \Delta \frac{dx}{dz}^{\text{geom}} \end{pmatrix} = \begin{pmatrix} 1 & 0 & -\frac{dx}{dz} & -y\frac{dx}{dz} & x\frac{dx}{dz} & -y \\ 0 & 0 & 0 & -\frac{dx}{dz}\frac{dy}{dz} & 1 + \left(\frac{dx}{dz}\right)^2 & -\frac{dy}{dz} \end{pmatrix} \begin{pmatrix} \delta_x \\ \delta_y \\ \delta_z \\ \delta_{\phi_x} \\ \delta_{\phi_y} \\ \delta_{\phi_z} \end{pmatrix} \quad (6)$$

Note that we no longer have any residual related to δ_y , so it is impossible to determine the y position of these chambers with any number of tracks. By an argument made in the introduction, it is also irrelevant, since we don't need to know the y position of these chambers to properly reconstruct tracks in them.

The situation for CSCs is similar to DT station 4, in that we only use two residuals components, $\Delta r\phi$ and $\Delta \frac{d(r\phi)}{dz}$. However, the fact that $r\phi$ is curvilinear implies that $\Delta r\phi$ residuals are sensitive to different combinations of δ_x and δ_y , depending on the x location of the track intersection. This leads to a more complicated transformation:

$$\begin{pmatrix} \Delta r\phi^{\text{geom}} \\ \Delta \frac{dr\phi}{dz}^{\text{geom}} \end{pmatrix} = \begin{pmatrix} 1 & \left[-\frac{x}{r} + 3\left(\frac{x}{r}\right)^3\right] & -\frac{dx}{dz} & -y\frac{dx}{dz} & x\frac{dx}{dz} & -y \\ 0 & -\frac{dx}{dz}/(2r) & 0 & \left[\frac{x}{r} - \frac{dx}{dz}\frac{dy}{dz}\right] & 1 + \left(\frac{dx}{dz}\right)^2 & -\frac{dy}{dz} \end{pmatrix} \begin{pmatrix} \delta_x \\ \delta_y \\ \delta_z \\ \delta_{\phi_x} \\ \delta_{\phi_y} \\ \delta_{\phi_z} \end{pmatrix}. \quad (7)$$

Sensitivity to δ_y is weak, suppressed by factors of x over the distance to the beamline r , because this is the component of $r\phi$ unit vectors in the local y direction. In practice, it is very difficult to extract this information from chambers without combining statistics.

To test these transformations, we constructed a pure-geometry toy Monte Carlo in the CMSSW framework. We propagated tracks to each muon chamber in the software's representation of the detector, before and after misaligning it. The differences in track intersections before and after misalignment are Δx^{geom} , Δy^{geom} , $\Delta \frac{dx}{dz}^{\text{geom}}$, and $\Delta \frac{dy}{dz}^{\text{geom}}$. Use of the official framework ensures that all conventions conform to those used in the actual alignment. Geometric residuals computed this way responded to misalignments exactly as described by Eqns 5–7, for symmetric and asymmetric distributions of track parameters $(x, y, \frac{dx}{dz}, \frac{dy}{dz})$, single-parameter misalignments and random sets of multi-parameter misalignments.

To test the fit function that we will describe in the next section, we added small Gaussian measurement errors to the residuals and applied the fitter to it as though it were data. The fitter returned the correct input misalignments for thousands of randomly-generated trials. Figs 6 and 7 present diagnostic plots from the fitter.

2.4 Fitting the residuals distribution

In the real detector, measurement error contributions to the residuals are much larger than the systematic distortions we seek to correct. It is therefore necessary to have a realistic description of the shape of the measurement error's distribution, so that we can extract

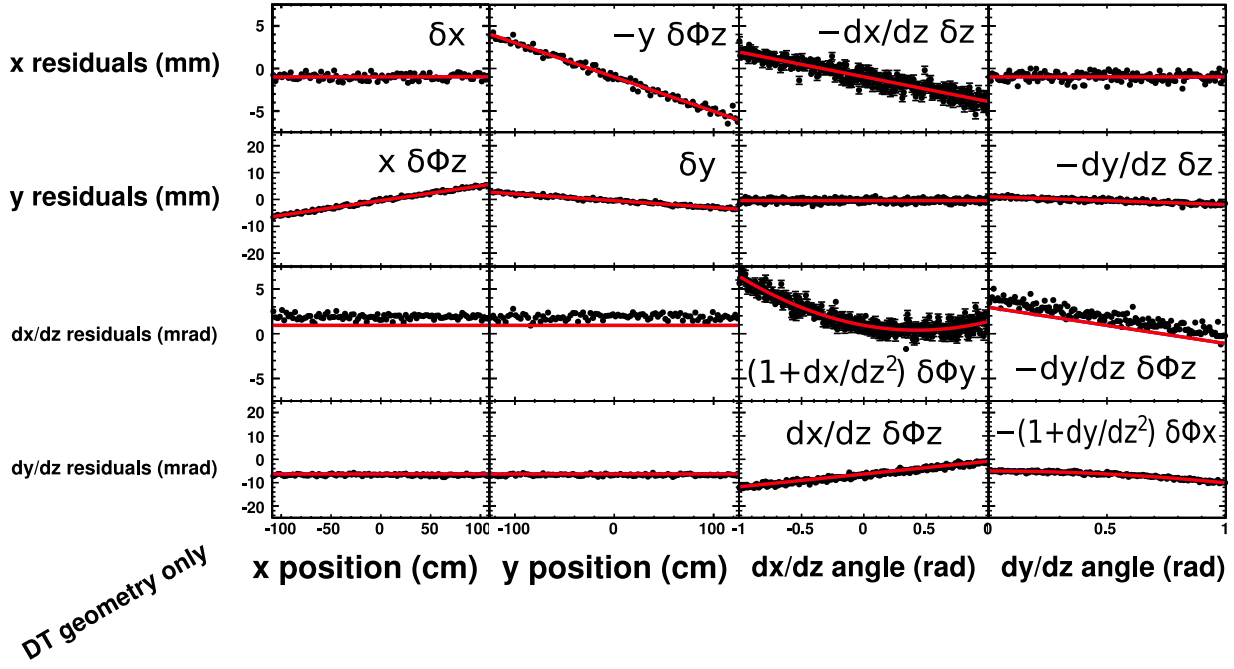


Figure 6: An example of a fit to 6 misalignment degrees of freedom in a “pure geometry” DT simulation with only small Gaussian measurement errors. Points are profile histograms of the four residuals versus the four track parameters. Lines are restrictions of the fit function with all parameters set to zero except the one shown. The $\Delta \frac{dx}{dz}$ profiles differ from their fit lines because the mean of the distribution does not exactly describe its value at zero. Annotations highlight the most significant contribution to each plot.

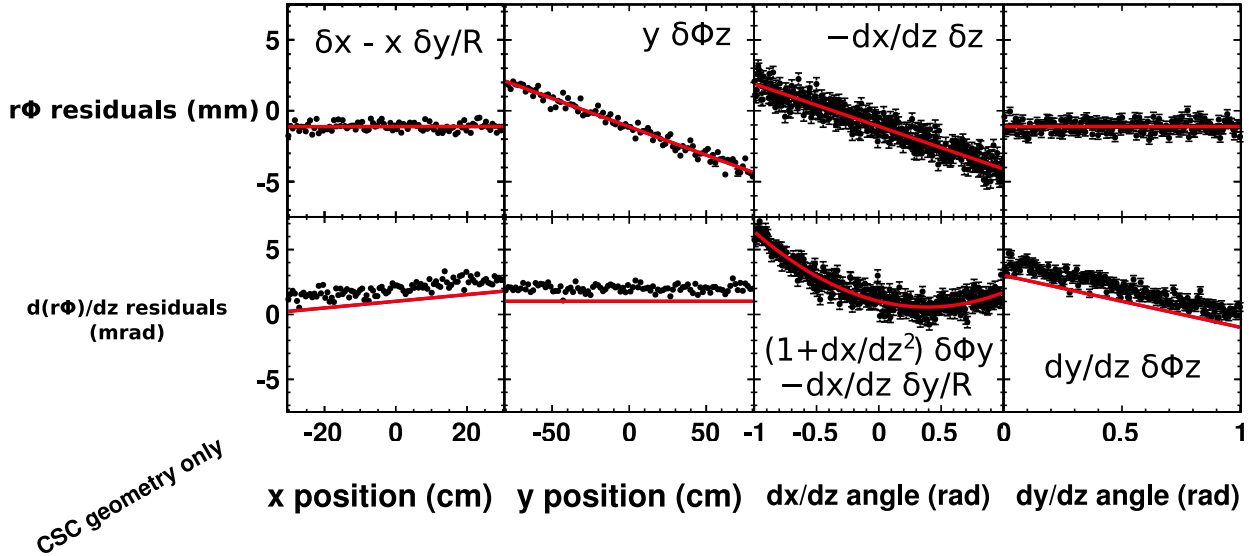


Figure 7: A “pure geometry” CSC simulation; see the caption of Fig 6 for details.

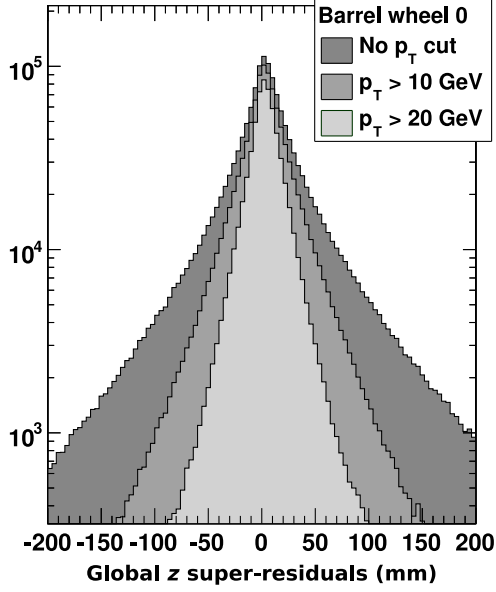


Figure 8: Histogram of residuals in log scale to highlight power-law tails. Low-momentum muons are more likely to scatter; hence applying a p_T cut varies the tails more than the central Gaussin.

alignment corrections from a global fit to all the parameters that influence residuals on a chamber. The measurement effects are:

- statistical error from the track-fit, amplified by the long propagation from Reference to Target (Gaussian),
- multiple-scattering in material (Gaussian),
- single-scattering in material (a bell curve with power-law tails, see Fig 8), and
- detector resolution (Gaussian and much smaller than the above).

The exact power of the single-scattering tail shape, including any asymmetries it might have, is not significant to the fitted value of the peak because the Gaussian errors dominate. We choose to describe the single-scattering with a Cauchy-Lorentz distribution. To model all of the effects, we use a convolution of the two distributions,

$$f(x; x_0, \sigma, \gamma) = \int_{-\infty}^{\infty} \frac{1}{\pi} \frac{\gamma}{(x - \xi - x_0)^2 + (\gamma)^2} \times \frac{1}{\sqrt{2\pi}\sigma} \exp\left(\frac{-\xi^2}{2\sigma^2}\right) d\xi, \quad (8)$$

also known as a Voigt distribution (Fig 9). We will describe how this function is applied to residuals momentarily.

Another important effect is the correlation between Δx and $\Delta \frac{dx}{dz}$ and the correlation between Δy and $\Delta \frac{dy}{dz}$. Position and angular residuals are correlated because an angular error early in a track's propagation causes it to accumulate position error, as presented in

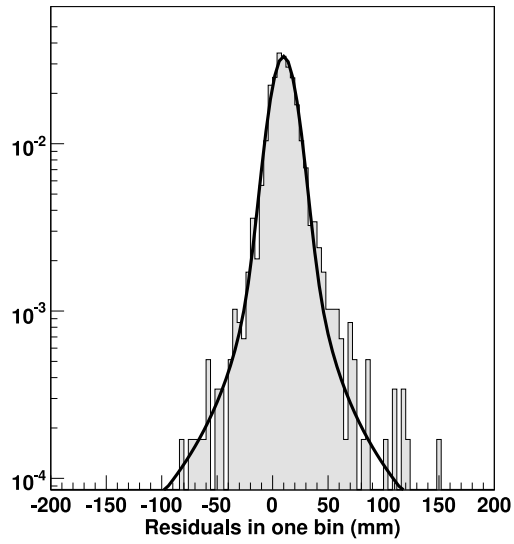


Figure 9: Fit function for residuals with a Gaussian core and power-law tails. The residuals in this plot were selected from a geographically small region of the detector (within DT station 4, wheel 0) to avoid smearing from misalignment.

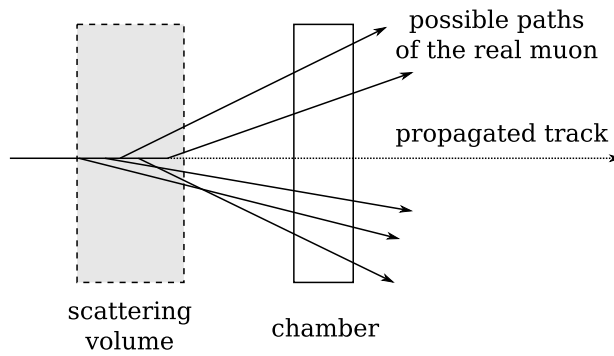


Figure 10: Correlation between position residual and angular residual.

Fig 10. The correlation is strongest at the furthest point from the Reference volume or scattering volume which introduced the error.

A chamber with four residuals components is fitted to the following four functions simultaneously:

$$f_{\Delta x} \left(\Delta x, \Delta \frac{dx}{dz}, x, \frac{dx}{dz}, y, \frac{dy}{dz}; \delta_x, \delta_y, \delta_z, \delta_{\phi_x}, \delta_{\phi_y}, \delta_{\phi_z}, \sigma_{\Delta x}, \gamma_{\Delta x}, \alpha_{\Delta x} \right) = f \left(\Delta x; \Delta x^{\text{geom}} \left(x, \frac{dx}{dz}, y, \frac{dy}{dz}, \delta_x, \delta_y, \delta_z, \delta_{\phi_x}, \delta_{\phi_y}, \delta_{\phi_z} \right) + \alpha_{\Delta x} \Delta \frac{dx}{dz}, \sigma_{\Delta x}, \gamma_{\Delta x} \right) \quad (9)$$

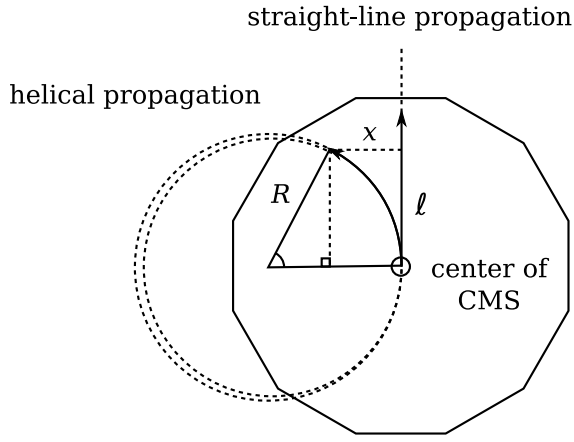
$$f_{\Delta \frac{dx}{dz}} \left(\Delta \frac{dx}{dz}, x, \frac{dx}{dz}, y, \frac{dy}{dz}; \delta_x, \delta_y, \delta_z, \delta_{\phi_x}, \delta_{\phi_y}, \delta_{\phi_z}, \sigma_{\Delta \frac{dx}{dz}}, \gamma_{\Delta \frac{dx}{dz}} \right) = f \left(\Delta \frac{dx}{dz}; \Delta \frac{dx}{dz}^{\text{geom}} \left(x, \frac{dx}{dz}, y, \frac{dy}{dz}, \delta_x, \delta_y, \delta_z, \delta_{\phi_x}, \delta_{\phi_y}, \delta_{\phi_z} \right), \sigma_{\Delta \frac{dx}{dz}}, \gamma_{\Delta \frac{dx}{dz}} \right) \quad (10)$$

$$f_{\Delta y} \left(\Delta y, \Delta \frac{dy}{dz}, x, \frac{dx}{dz}, y, \frac{dy}{dz}; \delta_x, \delta_y, \delta_z, \delta_{\phi_x}, \delta_{\phi_y}, \delta_{\phi_z}, \sigma_{\Delta y}, \gamma_{\Delta y}, \alpha_{\Delta y} \right) = f \left(\Delta y; \Delta y^{\text{geom}} \left(x, \frac{dx}{dz}, y, \frac{dy}{dz}, \delta_x, \delta_y, \delta_z, \delta_{\phi_x}, \delta_{\phi_y}, \delta_{\phi_z} \right) + \alpha_{\Delta y} \Delta \frac{dy}{dz}, \sigma_{\Delta y}, \gamma_{\Delta y} \right) \quad (11)$$

$$f_{\Delta \frac{dy}{dz}} \left(\Delta \frac{dy}{dz}, x, \frac{dx}{dz}, y, \frac{dy}{dz}; \delta_x, \delta_y, \delta_z, \delta_{\phi_x}, \delta_{\phi_y}, \delta_{\phi_z}, \sigma_{\Delta \frac{dy}{dz}}, \gamma_{\Delta \frac{dy}{dz}} \right) = f \left(\Delta \frac{dy}{dz}; \Delta \frac{dy}{dz}^{\text{geom}} \left(x, \frac{dx}{dz}, y, \frac{dy}{dz}, \delta_x, \delta_y, \delta_z, \delta_{\phi_x}, \delta_{\phi_y}, \delta_{\phi_z} \right), \sigma_{\Delta \frac{dy}{dz}}, \gamma_{\Delta \frac{dy}{dz}} \right) \quad (12)$$

That is, the residuals are fitted to four Voigt distributions whose peak value is the geometric residuals. The geometric residuals depend on track parameters $x, y, \frac{dx}{dz}, \frac{dy}{dz}$ and the 6 alignment parameters through Eqns 5–7. The position-residual distributions include a parameterized offset proportional to its corresponding angular residual, a skew factor which allows the Voigt error ellipse to tilt an angle $\tan^{-1}(\alpha)$ in $(\Delta x, \Delta \frac{dx}{dz})$ space without changing the normalization of the function. The product of the four functions 9–12 expresses the likelihood of a $(\Delta x, \Delta \frac{dx}{dz}, \Delta y, \Delta \frac{dy}{dz})$ super-residual as a function of the parameters, including the 6 alignment parameters. We perform a weighted, unbinned maximum likelihood fit for all of the parameters with MINUIT [6]. The weights are the $(\chi^2/\text{ndf})^{-1}$ of the super-residuals, with the smallest 1% of χ^2/ndf values excluded to avoid spikes in the distribution.

Though it may seem procedurally complicated, this is functionally a minimal modification of the HIP procedure used to align the tracker [4]. In the tracker's HIP procedure, the peak of the residuals distribution is determined by a weighted mean, which is equal to a weighted, unbinned maximum likelihood fit to a Gaussian. The difference in our case is that we allow for long tails in the distribution due to single-scattering. The long tails in the fit function reduce the contribution of outliers to the likelihood calculation, and thus reduce the influence



(a) Diagram for derivation: x is the displacement between straight and helical propagation of a track with radius of curvature R at a distance ℓ from the interaction point. If the field is mis-modelled, it would contribute $\Delta x^{\text{mag}} = x_{\text{track}} - x_{\text{muon}}$ to the residual, the difference of two helical propagations with different radii.

Displacement from straight propagation:

$$x = R (1 - \cos(\sin^{-1}(\ell/R)))$$

$$x \approx R \left(\frac{1}{2} (\ell/R)^2 \right) = \frac{\ell^2}{2R}$$

Relationship to magnetic field B_z :

$$R = \frac{\ell^2}{2x} = 300 \text{ cm T/GeV} \frac{p_T}{qB_z}$$

Residuals from field error ΔB_z :

$$\Delta x^{\text{mag}} = \frac{\ell^2}{2 \cdot 300 \text{ cm T/GeV}} \left(\frac{q}{p_T} \right) \Delta B_z$$

(b) Derivation of residuals dependence on q/p_T if the magnetic field is mis-modelled. If the B_z error is also non-uniform, the above holds with “ ΔB_z ” being a (non-trivial) quantity derived from field error along the track’s path.

Figure 11: If the z component of the magnetic field is poorly understood at the time of alignment, the error it contributes to residuals would be proportional to q/p_T .

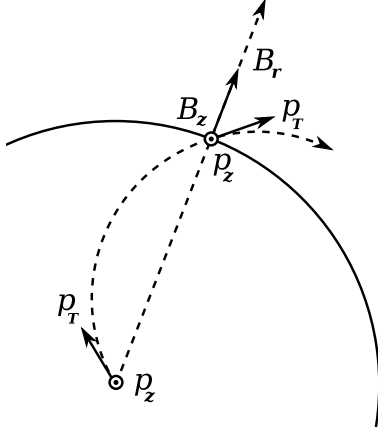
they have over the peak position. (This is why it is necessary to include tails even though the exact shape is not important.)

The fit is performed in a high-dimensional space with many parameters, which mandates caution. It is important to visually inspect the fit results, a topic which is raised in section 3.1 on validating the fit results.

2.5 Accomodating errors in magnetic field and material budget

Early in commissioning, track propagation through CMS may suffer from poor knowledge of the magnetic field map and material budget. This would result in incorrect residuals and potentially a wrong alignment. Since alignment is itself a commissioning task, it must be made independent of any propagation errors. Magnetic field and dE/dx errors from an incorrect material budget can be identified by their distinctive dependencies on momentum, and can both be cancelled by taking advantage of the fact that they affect residuals in a charge-antisymmetric way.

Fig 11 derives the effect of B_z (axial) errors on Δx residuals, which is proportional to q/p_T but not a simple function of the actual ΔB_z error. A similar derivation would reveal that residuals from B_r (radial) errors are proportional to q/p_z (Fig 12). Fig 13 derives the effect of B_z errors on $\Delta \frac{dx}{dz}$ residuals, which has a simpler dependence on magnetic field error, and could even be used to measure corrections to the field map.



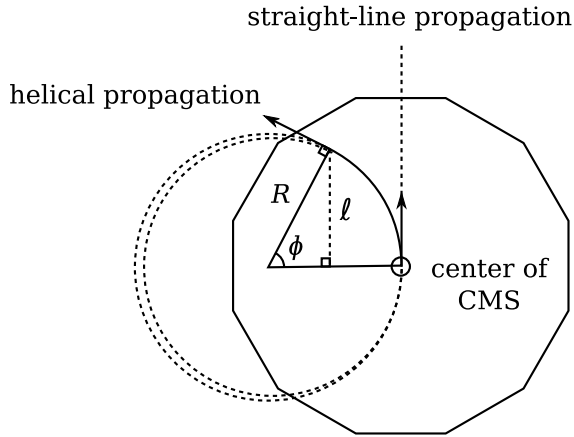
Components affecting $r\phi$ and ϕ_y residuals:

- $|\vec{p}_T \times \vec{B}_z| = |\vec{p}_T| |\vec{B}_z|$, always normal to trajectory
- $|\vec{p}_z \times \vec{B}_r| = |\vec{p}_z| |\vec{B}_r|$, approximately normal to trajectory at high momentum

Components affecting z and ϕ_x residuals:

- $p_T \times B_r$, negligible at high momentum

Figure 12: A summary of magnetic field components which affect residuals.



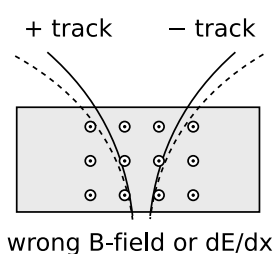
$$R = \frac{\ell}{\phi} = 300 \text{ cm T/GeV} \frac{p_T}{qB_z}$$

$$\Delta \frac{dx}{dz}^{\text{mag}} = \Delta \phi = \frac{\ell}{300 \text{ cm T/GeV}} \left(\frac{q}{p_T} \right) \Delta B_z$$

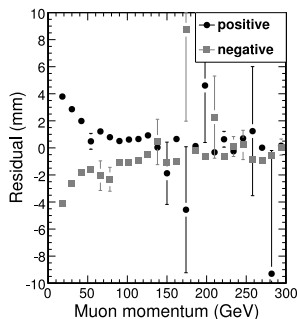
(a) Track angles are deflected $\phi = \sin^{-1} \ell/R \approx \ell/R$ relative to a straight-line propagation. If the magnetic field is mis-modelled, it would add $\Delta\phi = \phi_{\text{track}} - \phi_{\text{muon}}$ to the $\Delta \frac{dx}{dz}$ residual.

(b) Derivation of magnetic field contribution to $\Delta \frac{dx}{dz}$ residuals from mis-modelled B_z . If non-uniform, “ ΔB_z ” is a simple average of magnetic field error along the track’s path.

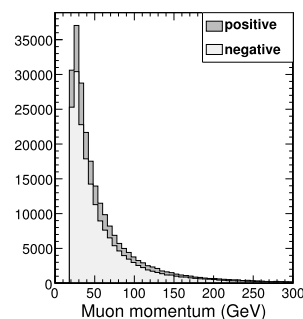
Figure 13: Magnetic field errors would also affect $\Delta \frac{dx}{dz}$ residuals, but in a simpler way.



(a) Both \vec{B} and dE/dx errors affect positive and negative muons in opposite ways.



(b) The two effects depend on momentum, but are still antisymmetric for charges in a given momentum bin.



(c) The momentum spectra for the two charges are proportional (cosmic rays shown above).

Figure 14: The two-bin method for cancelling \vec{B} and dE/dx errors: compute corrections separately for positive muons and negative muons, then average the two results.

Residuals from dE/dx errors have a different momentum dependence, but the same dependence on charge. In the momentum range of interest, the energy muons lose in material is independent of momentum: about $2 \text{ MeV cm}^2/\text{g}$, or 1.6 GeV/m through iron. The track propagator accounts for known material, so only errors in the material budget contribute to residuals. The errors may be positive or negative, depending on whether the material is overestimated or underestimated. Re-using the derivations in Figs 11 and 13, a constant correction to momentum $p_T \rightarrow (p_T - \Delta)$ yields a correction to Δx and $\Delta \frac{dx}{dz}$ residuals which is proportional to

$$qB_z \left(\frac{1}{p_T} - \frac{1}{p_T - \Delta} \right). \quad (13)$$

Thus the scaling of the effect is inversely quadratic in momentum, rather than inversely linear:

$$\frac{\frac{1}{p_1} - \frac{1}{p_1 - \Delta}}{\frac{1}{p_2} - \frac{1}{p_2 - \Delta}} = \frac{p_2}{p_1} \frac{1 - \left(1 - \frac{\Delta}{p_1}\right)^{-1}}{1 - \left(1 - \frac{\Delta}{p_2}\right)^{-1}} \approx \frac{p_2}{p_1} \frac{1 - \left(1 + \frac{\Delta}{p_1}\right)}{1 - \left(1 + \frac{\Delta}{p_2}\right)} = \left(\frac{p_2}{p_1}\right)^2 \quad (14)$$

In principle, we could determine all the alignment corrections, magnetic field errors, and dE/dx errors at once by adding dimensions and parameters to the fit function. However, that would unnecessarily reduce the statistical precision of our alignment measurement. Instead, we note that both types of propagation errors are antisymmetric with charge: positive and negative tracks would be deflected in opposite directions (opposite sign in the residuals contribution) by either effect (Fig 14(a)).

We account for magnetic field and dE/dx errors by computing alignment corrections separately in two bins, one filled with only μ^+ and the other filled with only μ^- . Residuals are biased by the \vec{B} and dE/dx errors as a function of momentum (Fig 14(b)), but since μ^+ and μ^- have similar spectra in cosmic rays and collisions (Fig 14(c)), the biases integrate to equal and opposite values in the two bins. The fitted alignment corrections, δ_+ and δ_- , are biased in equal and opposite ways, so we can compute unbiased corrections by averaging

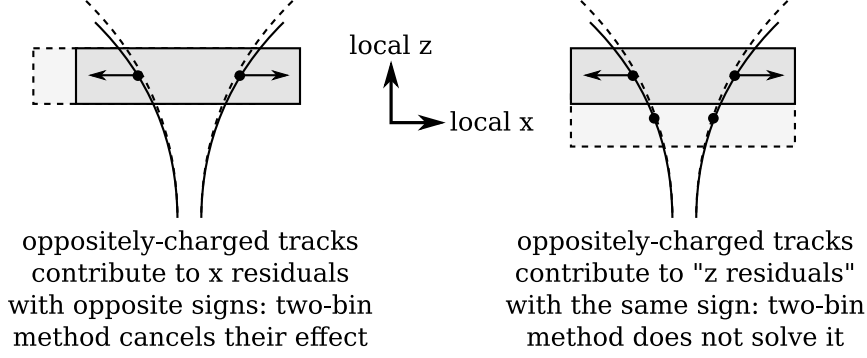


Figure 15: Why the two-bin method cannot correct for bias in δ_z .

them:

$$\text{final alignment corrections} = \frac{\delta_+ + \delta_-}{2}. \quad (15)$$

Moreover, we can trace the size of the correction, an overestimate of the systematic error, by monitoring the difference of the two:

$$\text{error tracer} = \frac{\delta_+ - \delta_-}{2}. \quad (16)$$

We call this the “two-bin” method for cancelling \vec{B} and dE/dx errors. It effectively scales up the least populated charge bin to cancel errors with the other charge bin.

An important caveat is that δ_z corrections require Δx residuals with opposite $\frac{dx}{dz}$ entrance angles to have opposite signs (see Eqn 5). Charge is highly correlated with $\frac{dx}{dz}$ entrance angle for geometric reasons, so this method is unable to correct for biases in δ_z (see Fig 15).

Positive and negative cosmic rays are known to have proportional spectra in our momentum range of interest: the charge ratio of cosmic secondaries is flat as a function of momentum. Most collisions muons also have this property, as b and \bar{b} are produced in equal abundance. Muons from W bosons may be asymmetric because W^+ and W^- are produced with different rates in pp colliders, but they are subdominant to b/\bar{b} .

Fig 16 demonstrates the robustness of the two-bin method in cosmic rays: a correction in the magnetic field map adjusts error tracer values, but not alignment residuals from the averaging technique.

3 Monitoring Tools and Validation/Verification

Visual monitoring of the alignment procedure is useful for two purposes: validation and verification. By “validation,” we mean simply checking that the procedure is valid, that it centers residuals distributions as intended. We will reserve the word “verification” for measurements that independently determine whether the aligned chamber positions accord with reality.

A generic example of validation would be to simply run the alignment procedure twice with the same tracks: if the second alignment yields zero corrections, then it validates the

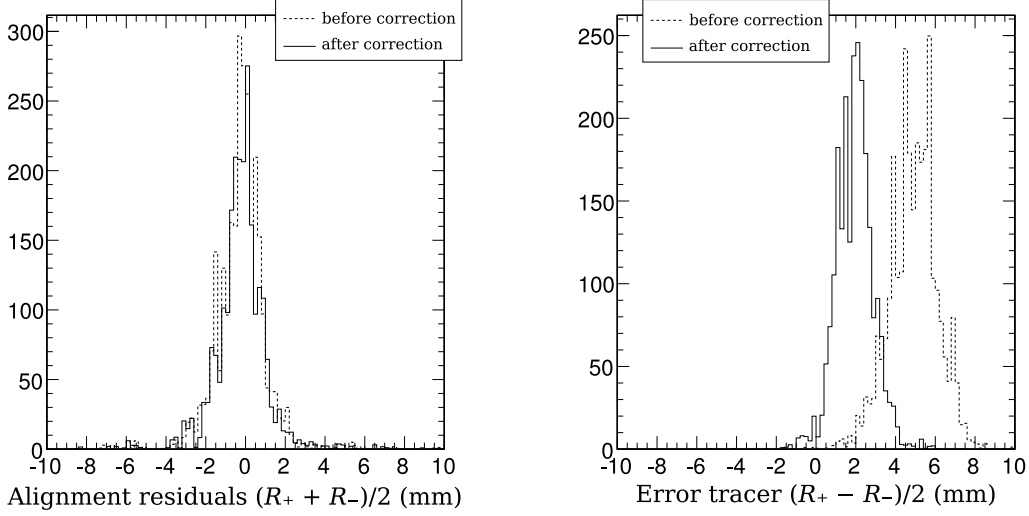


Figure 16: Alignment residuals and the error tracer before and after a correction to the magnetic field map (in DT station 4 with cosmic rays). The alignment residuals are unaffected by the large change in magnetic field values (20–30%).

first alignment. One way to actually verify the aligned positions would be to select three tracking volumes, A , B , and C , where A is used as a reference to align B and C , then B is used as a reference to align C with a different distribution of tracks. If the two procedures agree about the position of C , then C 's result has been independently verified as a real position in space.

Verification procedures do not need to be completely independent to be useful. As long as they contain some new information that is systematically distinct from the alignment procedure itself, they can add confidence to the measurement. Monitorable quantities range from pure validation to pure verification, and it will be important to keep in mind roughly how much new information each observable is giving us.

This section will focus on monitoring methods and show example plots, created under different circumstances, not necessarily the final alignment. For summary plots of alignment results, see sections 4 and 5. We only show a representative subsample of the detailed plots (which are by necessity numerous), while the summary plots contain the complete results.

3.1 Validating residuals fits

The alignment fits are performed in a high-dimensional space with many parameters, which is in principle dangerous. The fitter has a large space in which to find an unphysical minimum, and multi-dimensional data are hard to visualize quantitatively. Fortunately, our fit function has a shape that can be easily unfolded and plotted on a 2-D page. The fit function is a bell curve (Eqn 8) with the peak (x_0) being a multi-linear function of many variables. The multi-linear part can be regarded as a set of corrections to the peak position, which follows a line in parameter space, like the crest of a mountain ridge.

Fig 17 shows an example of residuals projections in Monte Carlo. The example was chosen as an extreme case, wheel ± 2 , station 1, where curves are least Gaussian. Projections have

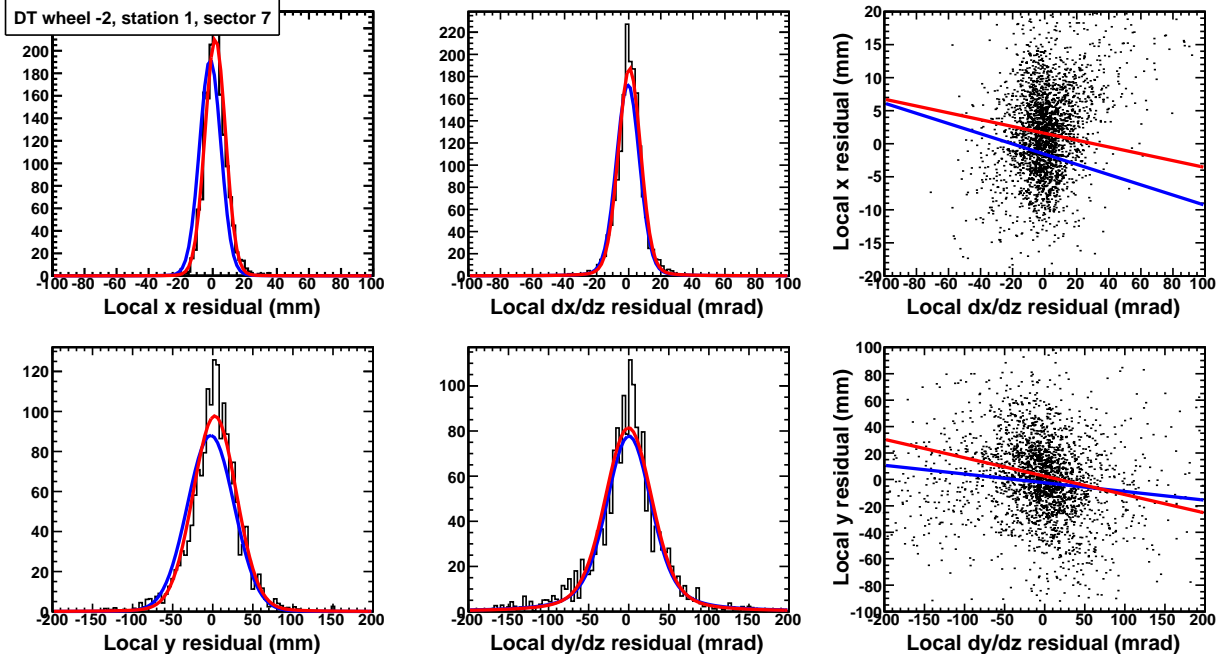


Figure 17: An alignment fit in Monte Carlo. Projections of the four residuals are presented along with a scatter plot showing the correlation between position and angular residuals. The red lines are fits to the μ^+ residuals (shown) and blue lines are fits to the μ^- residuals (not shown). The straight lines on the scatter plot indicate the correlation slope α .

all of the linear corrections applied to the peak residuals except for the constant offset, so that the fitted widths, σ and γ , will be relevant.

To study the corrections themselves, we plot each of the four residuals (Δx , $\Delta \frac{dx}{dz}$, Δy , and $\Delta \frac{dy}{dz}$) as a function of each of the four track parameters (x , $\frac{dx}{dz}$, y , and $\frac{dy}{dz}$). Fig 18 presents an example from misaligned Monte Carlo with the most important alignment corrections affecting each plot written on the plots. The example includes an “echo,” a misalignment trend from one distribution appearing in a different plot because of a correlation between track parameters, in this case between x and $\frac{dx}{dz}$. The correlation between these parameters is expected and illustrated in Fig 19. It also includes structure in Δy versus y , an effect not accounted for in the track reconstruction. After alignment (Fig 20), the echo is eliminated but the structure is not, because the structure is unrelated to any rigid body parameters.

3.2 Comparison of geometries in the database

3.3 Muon system maps

The fit-validation plots presented trends in residuals distributions inside each chamber. These trends were expected because they are caused by misalignments. However, if there are unexpected biases in the tracks used for alignment, either due to tracker misalignments or propagation errors, they would show up as trends in the residuals that cross chamber boundaries. To verify our expectation that residuals are correlated within each chamber and

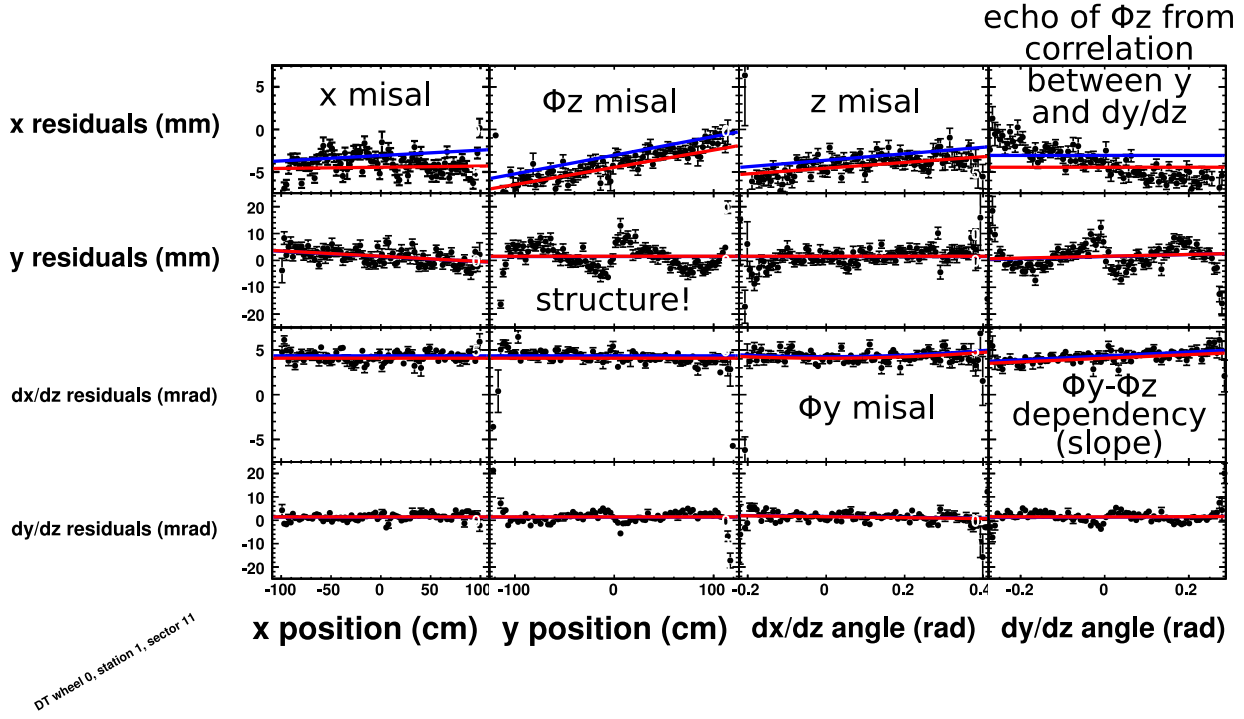


Figure 18: An annotated example of an alignment fit in Monte Carlo. Points are profile histograms of the four residuals versus the four track parameters. Lines are restrictions of the fit function with all parameters set to zero except the one shown. Red corresponds to the μ^+ fit and blue to the μ^- fit.

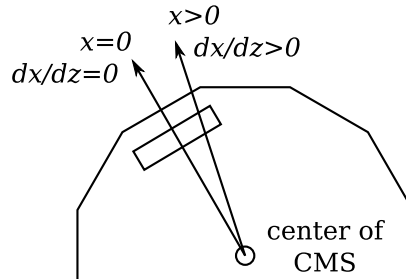


Figure 19: Expected correlation between x track intersections and $\frac{dx}{dz}$ entrance angles.

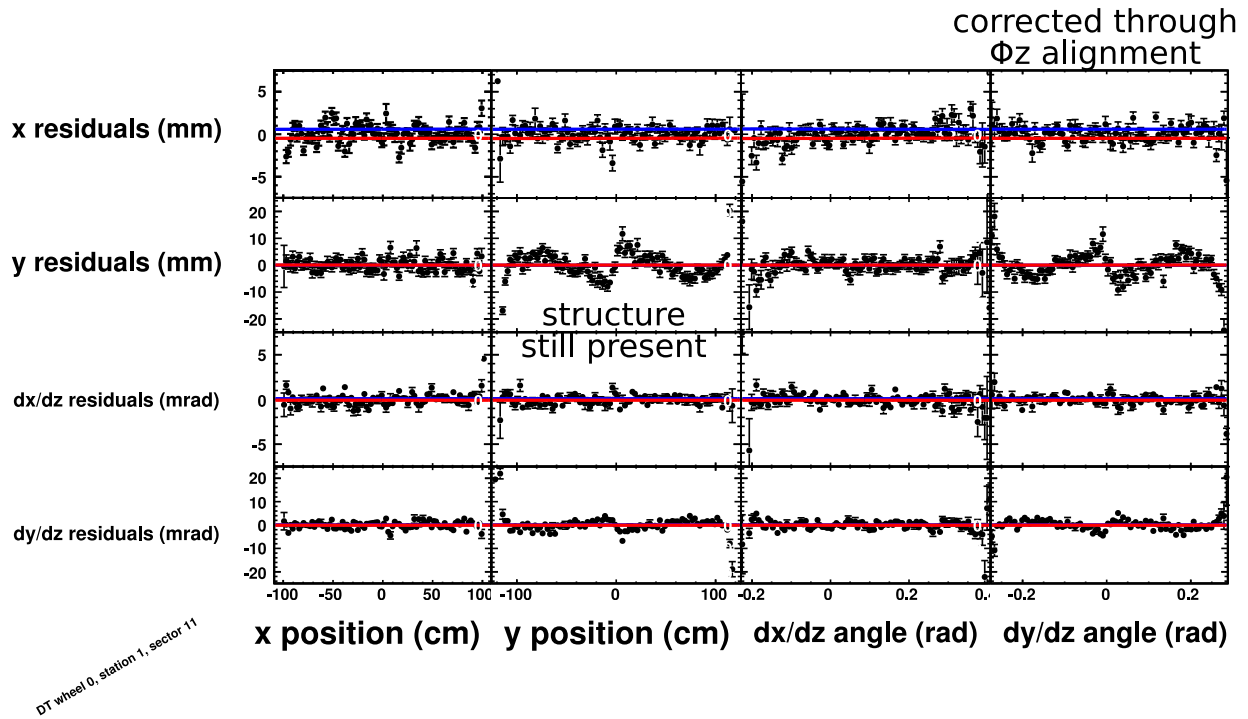


Figure 20: The same chamber as Fig 18 after alignment. “Echos” have disappeared because they are due to real alignment corrections in another parameter, but internal DT structure is irreducible with rigid body parameters.

uncorrelated outside, we plot maps of the residuals across the whole muon system.

The measurement planes of the DT chambers lie nearly flat in ϕ and z , so these are the relevant abscissas for the map plots. To make sure that no more than one chamber corresponds to each bin in the plots, the plots versus z must be split by sector, the plots versus ϕ must be split by wheel, and all plots must be split by station. The endcaps have 18 rings which are one CSC thick (counting ME1/1a as being distinct from ME1/1b), so each of these gets a separate ϕ plot. The CSCs lie flat in ϕ and the radial direction, instead of z , so the orthogonal plots are 36 radial spokes for each of the 8 disks. Some examples are shown in Fig 21.

On each of these axes, we plot all 6 alignment results: δ_x , δ_y , δ_z , ϕ_x , ϕ_y , and ϕ_z , as well as the antisymmetric combination of fit results to trace $\vec{B}(\vec{x})$ and dE/dx errors. Every bin is derived from the full fitting procedure described in section, though parameters equivalent to the binning are fixed. (Letting the slope of residuals versus x float in a dataset representing a narrow slice in x would statistically weaken all of the fit's results.) As with the fit-validation, there are too many plots to publish, but they are useful for diagnostics. An example of DT δ_z (radial displacement) in cosmic ray data is presented in Fig 22. This is a complicated quantity, the slope of fits to residuals versus track entrance angle, and it shows clear discontinuities at the chamber boundaries, indicating a real misalignment.

The muon system maps are the basis for binned-residual summary plots, where the points in the maps are used to fill a histogram, and therefore present all of the data on one page (trading depth for breadth). Such a plot is more incisive than a simple histogram of residuals, because pre-averaging the residuals in geographically relevant bins highlights systematic deviations from zero, rather than hiding it under track-by-track scattering. The width of the binned-residual distribution depends on the size of the bins, but they are standardized: 180 bins in ϕ from $-\pi$ to π , 60 bins in z from -660 cm to 660 cm (for DTs), and 60 bins in radial position, from 100 cm to 700 cm (for CSCs). Fig 16 from section 2.5 presented histograms of residuals binned in z .

3.4 Verification with relative residuals

The map plots provide some verification of the alignment in that they meaningfully compare residuals from the same chamber with residuals from neighboring chambers, and thus distinguish between distortions related to the chamber and distortions related to the tracks. However, they are the same residuals that were used to perform the alignment, and are therefore not independent.

Independent sets of residuals allow us to more fully verify the alignment by triangulation: after having aligned each chamber individually to the tracker, we check the alignment with residuals on tracks connecting the chambers themselves. One way to do this re-uses the alignment tracks, but ignores position information from the tracker. Consider the difference of residuals between two stations on each track, diagrammed in Fig 23:

$$\begin{aligned} \text{residuals difference}(3, 2) = & (\text{station 3 track impact point} - \text{station 3 hit position}) - \\ & (\text{station 2 track impact point} - \text{station 2 hit position}). \end{aligned} \quad (17)$$

The tracker's position information cancels in the residuals difference, as well as any ran-

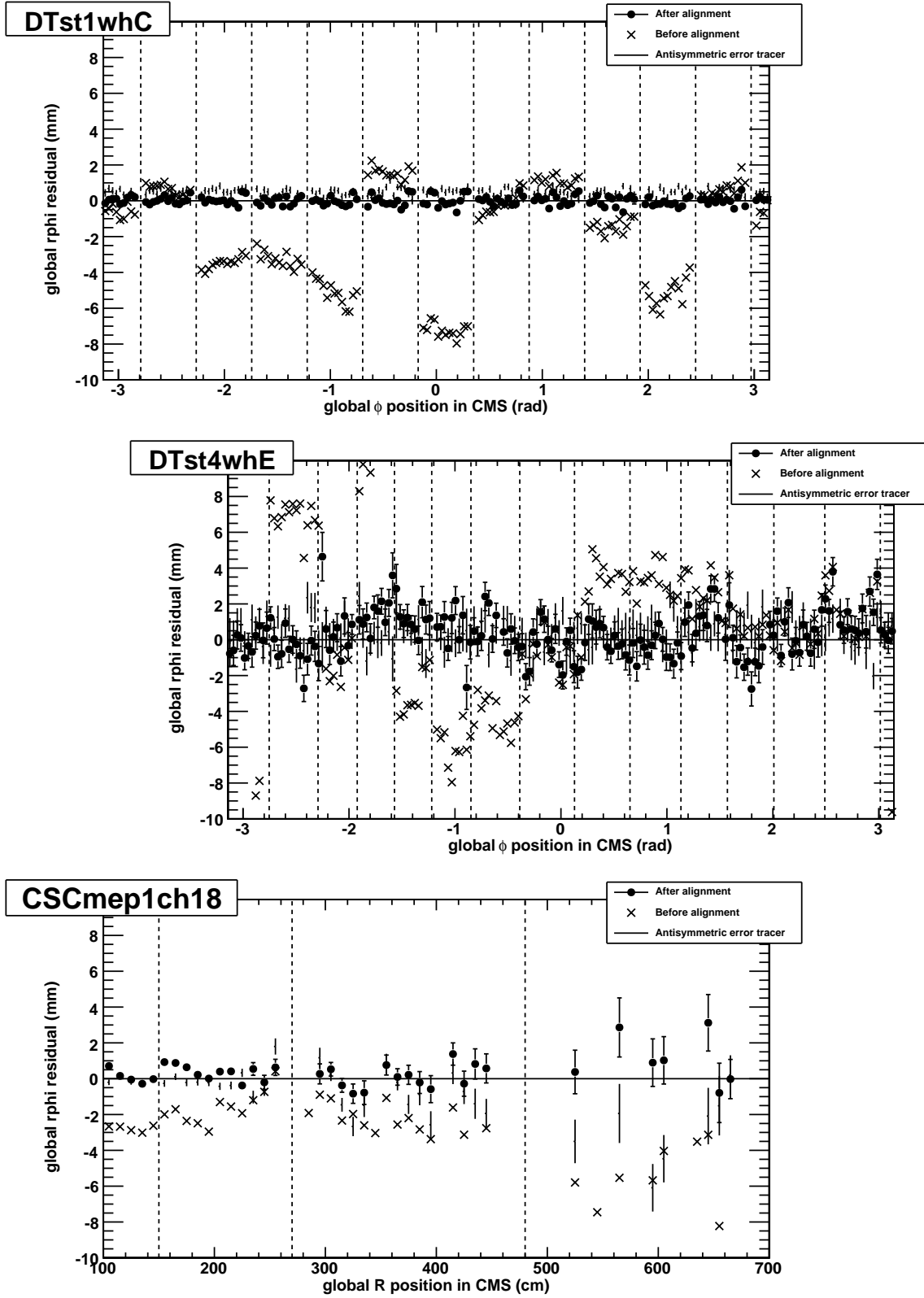


Figure 21: Three maps of residuals before and after alignment in Monte Carlo: DT station 1, wheel 0 (top), station 4 wheel +2 (middle), and CSC ME+1, chamber 18 (bottom). Chamber identities were not used to make the plots; boundaries are overlaid on the results.

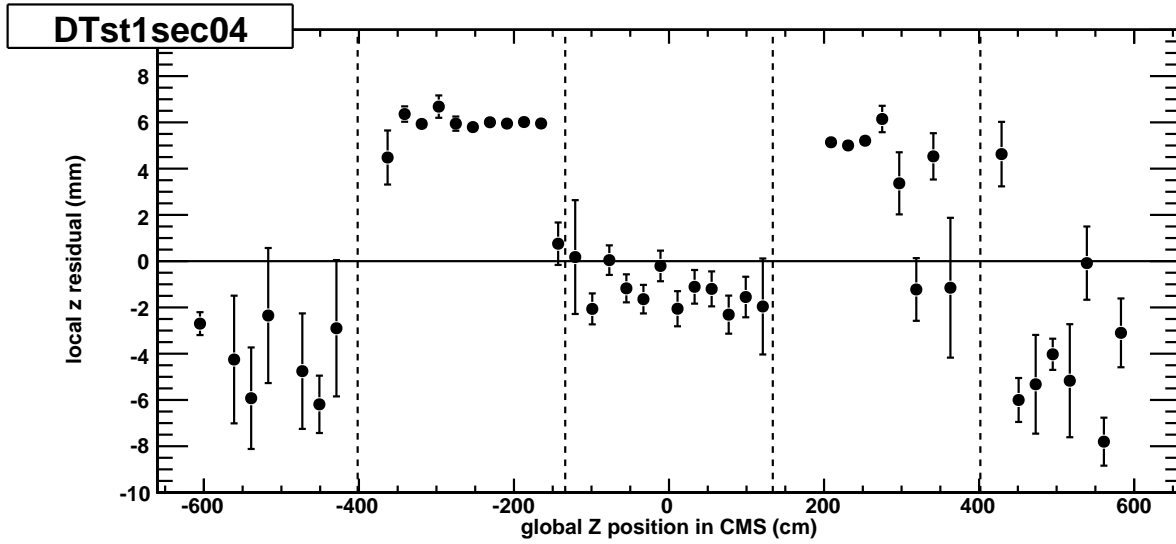


Figure 22: Results of δ_z fits (radial alignment for DT chambers) as a function of global z position. Results agree within each chamber and disagree with their neighbors, indicating real radial misalignments.

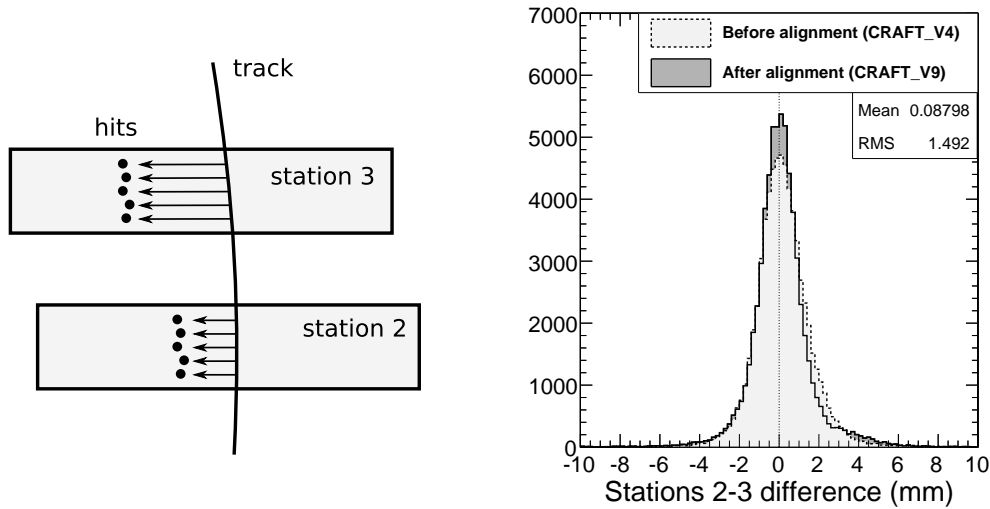


Figure 23: Relative residuals are linearly independent from the residuals used in alignment, and can therefore verify its correctness. PLACEHOLDER! This plot is from the old (3-parameter) CRAFT alignment. AND it is the only one that showed (marginal) improvement—stations 1–2 and 3–4 showed (marginal) degradation. (We interpret the three as indicating no net change in *relative* positions.) In the new plot, we will combine all stations, since they have comparable widths.

dom scattering that happens between the tracker and station 2. The residuals difference is therefore a narrower distribution than absolute residuals and represents the relative alignment of chambers in station 2 and chambers in station 3 (sector by sector). The advantage unique to this method is that the track retains momentum magnitude information from the tracker: it is a curved ruler, where the appropriate curvature is determined by the tracker's high-precision momentum measurement. The difference can be calculated for any pair of neighboring stations, but is difficult to interpret for DT stations 4 and 3, because the sector boundaries in station 4 do not line up with those in station 3.

A more extensive version of the same idea uses a set of aligned chambers as a new reference for track-fitting and re-aligning their neighbors. Chambers aligned by both methods verify the technique, though with less precision because the momentum resolution of the muon system is not as high as the tracker. Without collisions, this is the only way to align some chambers in the muon system, because the constraint requiring cosmic rays to pass through the tracker yields very few tracks in the high $|z|$ regions of the detector.

4 Global alignment results with collisions Monte Carlo

A study of alignment with 50 pb^{-1} of simulated muons from QCD (primarily $b \rightarrow \mu$, which is the majority of the muons that we'll see). I have the event samples in AlCaReco format, so it's ready to go. I've put it on hold until the tracker alignment is sufficiently well understood for us to do a combined alignment study which will become the new 50 and 200 pb^{-1} alignment scenarios.

4.1 Scaling with statistics

4.2 Dependence on tracker misalignment

4.3 Dependence on magnetic field errors

5 Global alignment results with cosmic ray data

I've described all of the method and plotting techniques, so this section will be light on text and heavy on plots with interpretations. I'm running the alignment now, and re-running it with small changes in the configuration to optimize our use of the data. I'll make all of the plots when I have a final alignment, ready to be used for tracker-pointing re-processing.

5.1 Validation plots

5.2 Verification with relative residuals

5.3 Verification with stand-alone muon alignments

This will take several weeks longer than everything else.

5.4 Verification with cosmic track splitting

Cosmic track splitting study by Nhan Tran and Alessio Bonato applied to global muons. It's independent because nothing in the alignment procedure explicitly correlated the top chambers with the bottom chambers. It will need to be repeated with the new alignment (as well as the new magnetic field, new tracker alignment, and new tracker weights). Naturally, they'll need to be acknowledged.

6 Relative alignment of CSCs with local tracks

We have focused so far on global alignment because of its importance in muon track-fitting, but local alignment methods have a different set of advantages which can be used to improve our overall understanding. Locally-propagated tracks, for instance from one chamber to its neighbor, suffer far less from propagation errors, yielding narrower residuals distributions and fewer systematic uncertainties. High precision can be achieved with fewer tracks because of the narrowness of the residuals, and the track source need not point to the tracker, so the endcap can be aligned before first collisions with beam-halo data. When collisions muons are available for the global alignment procedure, local alignment will severely test it and provide diagnostics in the case of a disagreement.

The disadvantage of local alignment algorithms is that they do not relate the coordinate frame of the aligned system to a common standard. In this section, we will describe a procedure that aligns CSCs within rings, but does not relate the aligned rings to each other or the tracker. Global muons from collisions will be required to make this connection, though we can combine residuals from all the chambers in each ring to minimize statistical uncertainty and average over possible systematic effects.

6.1 Description of the CSC Overlaps algorithm

In the muon endcap, CSCs were designed to overlap slightly with their neighbors for the purpose of local alignment. In each ring except ME1/3, tracks on the left edge of chamber i can be expected to also pass through the right edge of chamber $i + 1$, so both chambers can independently determine the track parameters with all 6 layers. If these chambers systematically disagree about the positions of tracks in a shared coordinate system, then one or both are misaligned. Relative alignment corrections can be propagated through the ring until we return to the first chamber, at which point the collection of chambers must form a consistent circle, a constraint known as closure.

This can be made more formal by defining $N = 18$ or 36 alignment corrections A_i (where $i \in \{1 \dots 18\}$ for ME2/1, ME3/1, ME4/1 and $i \in \{1 \dots 36\}$ for the other stations). The ring also has N residuals distributions, but each residuals distribution corresponds to a pair of chambers, not an individual chamber, because each residual is the position of the track as measured in chamber i minus the position of the track as measured in chamber $i + 1$. (Index arithmetic should be presumed to be mod N , such that $i + 1 = 1$ when $i = N$. Remember that the chambers are arranged in a circle.) To use the language of the preceding sections in this note, we may think of one chamber as the reference tracking volume and the other as the target to be aligned, except that there is no reason to prefer one as a reference above

the others. Label the mean of the residuals distribution corresponding to chambers i and $i + 1$ as $\alpha_{i, i+1}$. We can use the mean of the residuals distribution, rather than a fit for its peak, because scattering is not an issue.

If we move chambers i and $i + 1$ by A_i and A_{i+1} , the mean of the overlap residuals can be expected to change from $\alpha_{i, i+1}$ to $\alpha_{i, i+1} - (A_i - A_{i+1})$. We want to find a complete set of corrections to minimize all of the residuals means, so we define a χ^2 as

$$\chi^2 = (\alpha_{12} - A_1 + A_2)^2 + (\alpha_{23} - A_2 + A_3)^2 + \dots + (\alpha_{N1} - A_N + A_1)^2 \quad (18)$$

and minimize it by setting its derivatives to zero. For example,

$$\frac{1}{2} \frac{\partial \chi^2}{\partial A_2} = (\alpha_{12} - A_1 + A_2) - (\alpha_{23} - A_2 + A_3) = 0. \quad (19)$$

The complete set of such equations, written in matrix form, looks like the following (with $N = 5$ for brevity):

$$\begin{pmatrix} \alpha_{12} - \alpha_{51} \\ \alpha_{23} - \alpha_{12} \\ \alpha_{34} - \alpha_{23} \\ \alpha_{45} - \alpha_{34} \\ \alpha_{51} - \alpha_{45} \end{pmatrix} = \begin{pmatrix} 2 & -1 & & & -1 \\ -1 & 2 & -1 & & \\ & -1 & 2 & -1 & \\ & & -1 & 2 & -1 \\ -1 & & & -1 & 2 \end{pmatrix} \begin{pmatrix} A_1 \\ A_2 \\ A_3 \\ A_4 \\ A_5 \end{pmatrix}. \quad (20)$$

To align all N chambers, we need only invert this $N \times N$ matrix. We did not break the symmetry between the reference system and the target system: this procedure mutually aligns all chambers at once.

Unfortunately, the matrix in Eqn 20 is singular because a procedure like this cannot determine the global position of the whole system. Adding the same constant to every A_i , which would rotate the whole ring rigidly, would leave the χ^2 invariant because the relative positions of every pair of chambers is unchanged by the collective motion. Since there is a direction in $\{A_i\}$ -space in which χ^2 is flat, it cannot be minimized by setting its derivatives to zero. One way to solve the problem is to refuse motion in the flat direction by fixing one chamber, e.g. force $A_1 = 0$ and make chamber 1 the reference.

$$\begin{pmatrix} 0 \\ \alpha_{23} - \alpha_{12} \\ \alpha_{34} - \alpha_{23} \\ \alpha_{45} - \alpha_{34} \\ \alpha_{51} - \alpha_{45} \end{pmatrix} = \begin{pmatrix} 1 & 0 & 0 & 0 & 0 \\ -1 & 2 & -1 & & \\ & -1 & 2 & -1 & \\ & & -1 & 2 & -1 \\ -1 & & & -1 & 2 \end{pmatrix} \begin{pmatrix} A_1 \\ A_2 \\ A_3 \\ A_4 \\ A_5 \end{pmatrix} \quad (21)$$

However, if chamber 1 is misaligned, it would take the whole ring with it. Ring misalignments can be corrected later with global alignment, but it is best to avoid introducing them. Instead, we can make the flat direction quadratic in χ^2 by preferring $\{A_i\}$ sets that have an average of zero (minimally rotate the ring). This can be accomplished by adding a term like

$$\left[\frac{1}{N} (A_1 + A_2 + \dots + A_N) \right]^2 \quad (22)$$

to the χ^2 . Each derivative equation becomes

$$\frac{1}{2} \frac{\partial \chi^2}{\partial A_i} = (\alpha_{i-1, i} - A_{i-1} + A_i) - (\alpha_{i, i+1} - A_i + A_{i+1}) + \frac{1}{N^2} \sum_{i=1}^N A_i = 0, \quad (23)$$

so the matrix equation is now

$$\begin{pmatrix} \alpha_{12} - \alpha_{51} \\ \alpha_{23} - \alpha_{12} \\ \alpha_{34} - \alpha_{23} \\ \alpha_{45} - \alpha_{34} \\ \alpha_{51} - \alpha_{45} \end{pmatrix} = \left[\begin{pmatrix} 2 & -1 & & & -1 \\ & -1 & 2 & -1 & \\ & & -1 & 2 & -1 \\ & & & -1 & 2 \\ -1 & & & & -1 & 2 \end{pmatrix} + \frac{1}{N^2} \begin{pmatrix} 1 & 1 & 1 & 1 & 1 \\ 1 & 1 & 1 & 1 & 1 \\ 1 & 1 & 1 & 1 & 1 \\ 1 & 1 & 1 & 1 & 1 \\ 1 & 1 & 1 & 1 & 1 \end{pmatrix} \right] \begin{pmatrix} A_1 \\ A_2 \\ A_3 \\ A_4 \\ A_5 \end{pmatrix}. \quad (24)$$

It has a unique solution in which the average correction (Eqn 22) is minimized to exactly zero. Actually, adding any non-zero constant to every element would yield the same solution as the physically-motivated $\frac{1}{N^2}$.

The circular ring of chambers also provides an internal cross-check: the sum of the means of pairwise residuals must be zero. If not, no combination of alignment corrections can center all of the residuals, because

$$\text{closure} = \sum_{i=1}^N \alpha_{i, i+1} - (A_i - A_{i+1}) = \sum_{i=1}^N \alpha_{i, i+1} \quad (25)$$

is independent of $\{A_i\}$. (Note that $\sum_{i=1}^N A_{i+1}$ is just a reindexing of $\sum_{i=1}^N A_i$ because index arithmetic is understood to be mod N .) With non-zero closure, the solution of Eqn 24 uniformly distributes residuals so that they all have non-zero means, which is to say, every chamber disagrees with its neighbor about where the tracks are. Unclosed $r\phi$ residuals either imply

- the average distance of the chambers from the beamline is incorrect, or
- the presumed width of the chambers is incorrect.

In the first case, the circumference of the ring is miscalculated because the wrong radius is assumed; in the second case, the wrong arc is assumed per chamber. In the course of developing this technique, we discovered a 15 mm closure error, which derived from an 800 μm error in the active width of the chamber description, ultimately from a 0.09% error in the pitch angle of each cathode strip (10 μm per strip). It is a very sensitive technique!

6.2 Local CSC alignment parameters

As much as possible, the same techniques are used to calculate residuals and alignment corrections in the local procedure as in the global. Tracks propagated to a chamber are compared with the chamber's segment position and angle, much like the super-residuals described in section 2.2. Anode wire measurements are ignored due to their large granularity,

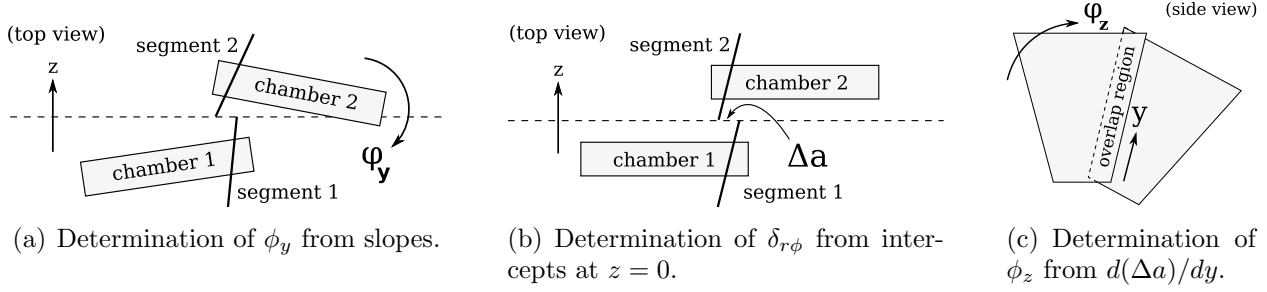


Figure 24: The three alignment parameters accessible to local track matching in CSCs.

and strips are taken to measure curvilinear $r\phi$ residuals, rather than cartesian local x , again in direct analogy with the global procedure. The difference is that the source for global tracks is the tracker, propagated through magnetic fields and many radiation lengths of material, while local tracks are extrapolations from a linear fit in the neighboring chamber. To treat the pair of chambers symmetrically, hits in each are fitted to line segments on the surface of a cylinder around the beamline

$$\phi(z) = a + bz \quad (26)$$

and the parameters of these two fits are compared at the plane equidistant between the chamber centers (at $z = (z_1 + z_2)/2$, where z_1 and z_2 are the global z positions of the two chambers).

Three parameters are accessible with this technique (Fig 24):

1. the relative ϕ_y of the two chambers is their average difference in slopes (Δb),
2. the relative $\delta_{r\phi}$ position is the difference in intercepts (Δa), and
3. the relative ϕ_z angle is the difference in intercepts as a function of hit position ($d(\Delta a)/dy$).

These parameters are interdependent in the sense that the $\delta_{r\phi}$ result depends on ϕ_y and the ϕ_z result depends on $\delta_{r\phi}$, but the dependencies are unidirectional. If corrected in the above order, first ϕ_y , then $\delta_{r\phi}$, then ϕ_z , the parameters decouple, avoiding the need for a combined fit.

The formalism developed in section 6.1 can be applied to each parameter separately. First, $\alpha_{i, i+1}$ is defined as $b_i - b_{i+1}$ and A_i as ϕ_{y_i} to align the angles, then $\alpha_{i, i+1}$ becomes $a_i - a_{i+1}$ and A_i becomes $\delta_{r\phi_i}$ to align the positions, and similarly for ϕ_z .

6.3 Specialized trigger and data streams

Only events with muons that thread the narrow overlaps between chambers are useful to this procedure, which is a small fraction of the whole. Beam-halo and collisions muons are equally useful, but they come from different sources (primary datasets) because they're reconstructed differently. We therefore have special triggers and data streams for each case, to avoid losing events to generic prescales.

Four triggers are designed to accept beam-halo events. They are

- HLT_CSCBeamHalo: simply passes L1_SingleMuBeamHalo bit, likely to be prescaled,
- HLT_CSCBeamHaloRing2or3: same but additionally requires reconstructed hits in $ME_n/2$ or $ME_1/3$, which are less common and therefore deserve a lower prescale,
- HLT_CSCBeamHaloOverlapsRing1 and Ring2: requires clusters of reconstructed hits in neighboring chambers, consistent with a muon in the overlap region.

Naturally, the two specialized overlaps triggers are essential to the CSC Overlaps procedure; the others are for cross-checks and detector studies which may be unrelated to alignment. To produce one complete $ME_n/1$ alignment per day, we would need 0.4 Hz from HLT_CSCBeamHaloOverlapsRing1, and for one $ME_n/2$ alignment per day, we would need 0.8 Hz from HLT_CSCBeamHaloOverlapsRing2 (scaling from 2008 exercise).

Events with beam-halo trigger bits are then collected by the MuAlBeamHaloOverlaps AlCaReco stream (similar to MuAlCalIsolatedMu, MuAlGlobalCosmics, and MuAlStandAloneCosmics, discussed on page 9). MuAlBeamHaloOverlaps has no explicit p_T cut (the momentum of tracks parallel to \vec{B} would not be measured well anyway), with an option to apply a coarse energy cut by requiring the reconstructed track to pass through a given number of stations.

Collisions muons to be used with the CSC Overlaps procedure are collected with the standard single-muon triggers and whatever prescales that implies (in flux at the low end of the momentum scale). They are then delivered to alignment via the MuAlOverlaps stream. As usual, the AlCaReco streams contain only what is needed for alignment: tracks and the hits associated with those tracks, so they use very little disk space for the number of events they contain.

6.4 Results from the 2008 LHC run

On September 10–17, 2008, protons circulated in the LHC tunnel, providing a source of beam-halo muons which we used to test the CSC Overlaps procedure. Three-quarters of the beam-halo events were collected from a 9-minute run on the evening of September 11 (run number 60232; 33,000 HLT_CSCBeamHaloOverlapsRing1 triggers). To guarantee a consistent snapshot of the detector geometry, we select data from this run only. The CSC Overlaps procedure is only meaningful when applied to rings in which all chambers are actively taking data; missing data in any one chamber removes two residuals constraints (e.g. $\alpha_{i-1, i}$ and $\alpha_{i, i+1}$), making Eqn 24 unsolvable. In this run, $ME-2/1$ and $ME-3/1$ were the only completely-active rings (the beam was coming from the minus side of CMS, which contributed significantly more muons to the minus endcap). Many of the CSC commissioning problems experienced in 2008 have been fixed in the long shut-down, so we can expect more complete rings in 2009.

The procedure was first applied to beam-halo Monte Carlo with approximately the same number of events but a different azimuthal and radial distribution than the real beam. (The azimuthal and radial distribution of the real beam varied considerably from run to run, more than the difference between our chosen run and the Monte Carlo.) Fig 25 presents the results from a simulated alignment procedure, starting from a standard misaligned geometry (2008 “STARTUP” scenario). The standard deviation of the difference between aligned chamber

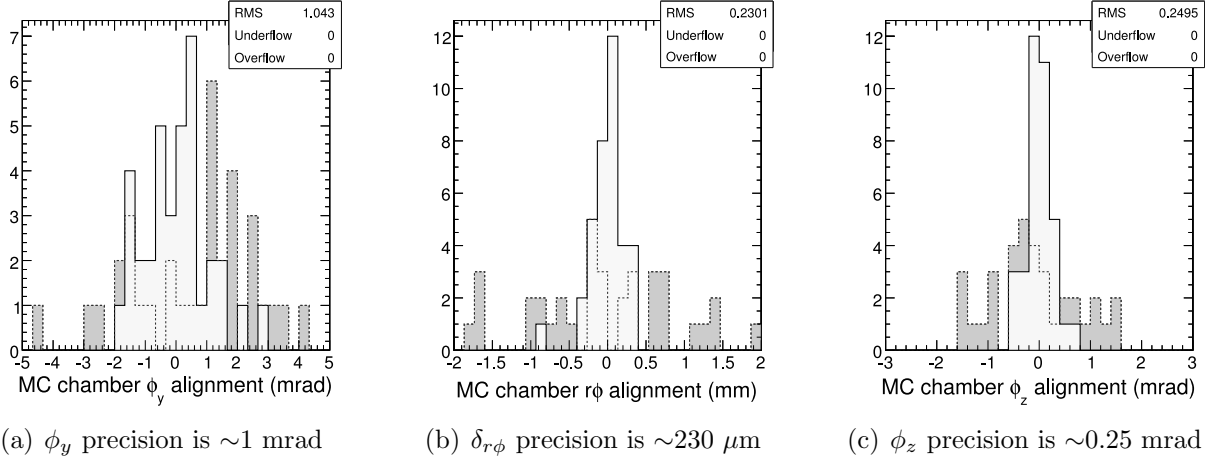


Figure 25: Comparison of alignment parameters with MC truth before (dark) and after (light) a simulated beam-halo alignment with similar statistics to the 2008 LHC run.

positions and MC truth quantifies the precision of the technique, though the interpretation is approximate because of the differences in track distribution.

To verify the aligned positions of chambers in real data, we compare the beam-halo results with photogrammetry, an alignment derived from a literal photograph of the detector. Each chamber has two alignment pins, connected directly to the active layer planes and capped with a reflective disk, the center of which is accurately measured by the photographs. An average of the two pin positions yields the $r\phi$ location of the chamber and a difference of the two pin positions, divided by the distance between the pins, yields the ϕ_z angle. The ϕ_y angle is inaccessible to photogrammetry, because both pins lie on the chamber's local y axis. The photogrammetry results are clearly independent from the track-based results, and can therefore be used to verify the latter. The beam-halo data were collected with no magnetic field, just like the photogrammetry, so we can be confident that they describe the same geometry.

Fig 26 presents the aligned value of each parameter of each chamber relative to ideal values for both track-based alignment and photogrammetry. One can see that the two methods are both measuring significant differences with respect to ideal, and that the results are highly correlated.

To compute the accuracy of the beam-halo alignment with photogrammetry as the reference, we subtract the $\delta_{r\phi}$ and ϕ_z of each beam-halo result from the corresponding photogrammetry result (Fig 27). The mean (bias) is consistent with zero, but in the $\delta_{r\phi}$ case, a non-zero mean would correspond to a global rotation of the disk which is not a measurable parameter in the CSC Overlaps procedure or the single-disk photogrammetry. The standard deviations are $340 \mu\text{m}$ in $\delta_{r\phi}$ and 0.42 mrad in ϕ_z , which derive from a sum in quadrature of the track-based uncertainties and the photogrammetry uncertainties. Photogrammetry uncertainties are $300 \mu\text{m}$ for each pin [5], which means $(300 \mu\text{m})/\sqrt{2} = 210 \mu\text{m}$ for the chamber center position and $(300 \mu\text{m}) \cdot \sqrt{2}/1.85 \text{ m} = 0.23$ mrad for the chamber angle. Subtracting the photogrammetry uncertainties in quadrature from standard deviations observed in the

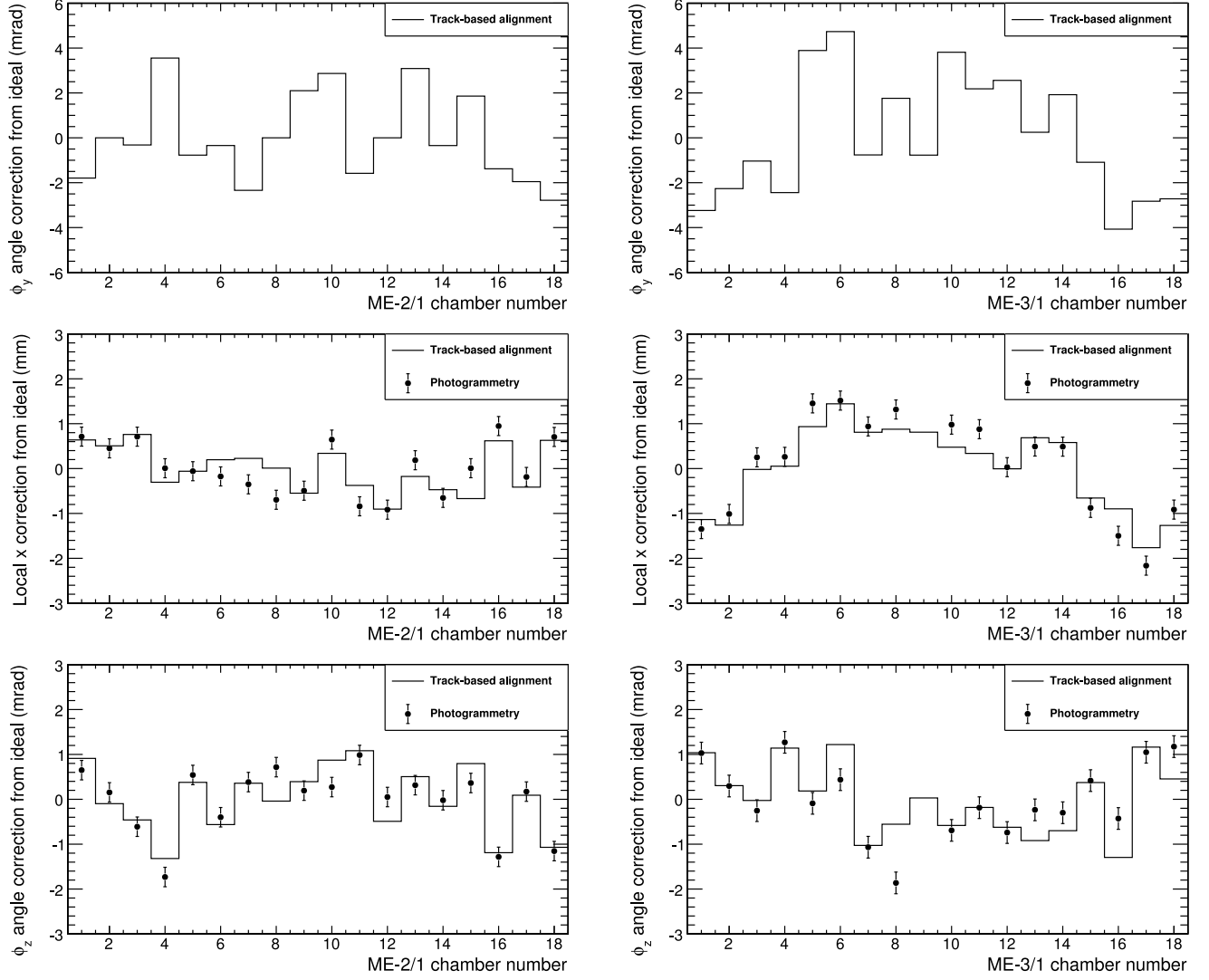


Figure 26: CSC alignment results from the Overlaps procedure and the 2008 LHC run, presented as a difference from ideal and compared with photogrammetry where possible.

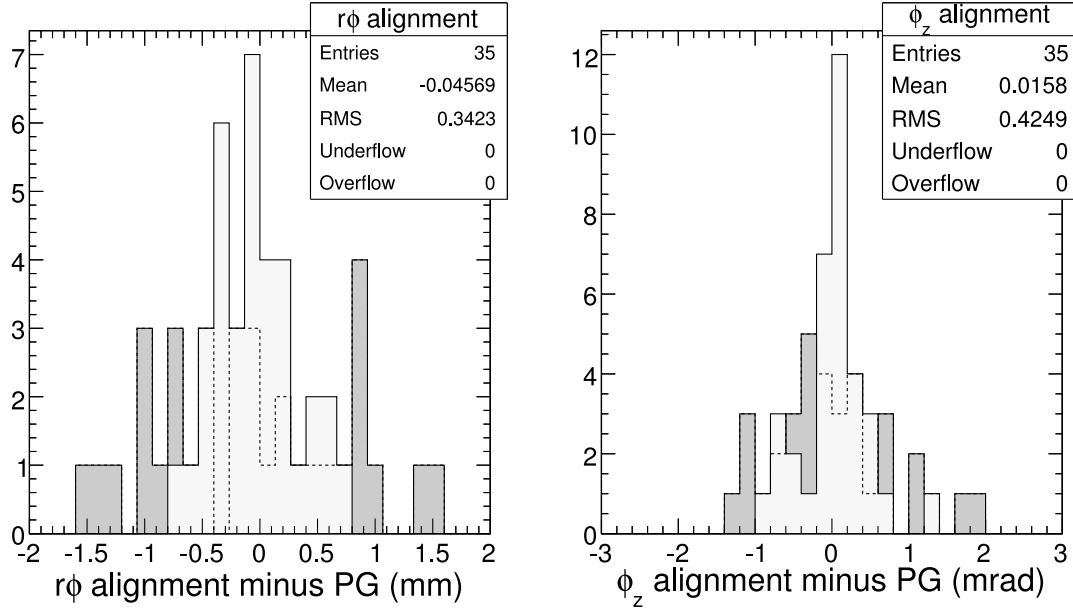


Figure 27: Chamber-by-chamber verification of the beam-halo alignment with photogrammetry. The dark histogram is before alignment; the light histogram and statistics box are after alignment.

plots,

$$\text{track-based } \delta_{r\phi} \text{ accuracy} = \sqrt{(340 \mu\text{m})^2 - (210 \mu\text{m})^2} = 270 \mu\text{m} \quad (27)$$

$$\text{track-based } \phi_z \text{ accuracy} = \sqrt{(0.42 \text{ mrad})^2 - (0.23 \text{ mrad})^2} = 0.35 \text{ mrad} \quad (28)$$

Thus, the 200-300 μm accuracy goals are already demonstrated in a subset of endcap chambers, using a local alignment technique. There is no indication that this result is systematically limited; much higher precision may be possible once we collect more than 12 minutes of data.

6.5 Extension to align CSC layers

The CSC Overlaps procedure can be extended to align CSC layers, though the layer procedure only needs to be applied once with high statistics, rather than routinely with a maintainable algorithm. The usual difficulty in aligning layers with local tracks is that the systems are underconstrained. Extra constraints applicable to tracks overlapping well-aligned neighbors allow us to break all of the important degeneracies.

Local alignment procedures require tracks to be fitted locally, which introduces an interdependency between track-fitting and alignment. In the CSC Overlaps procedure, we needed the circular closure constraint to form an overconstrained system, and no such thing is available inside of a chamber. In a chamber, there are 6 layers; in principle, 5 need to be aligned, since the collective position of all the layers is a chamber-alignment issue. But it takes at least 2 parameters to determine each track: one too many. If we simply ignore this

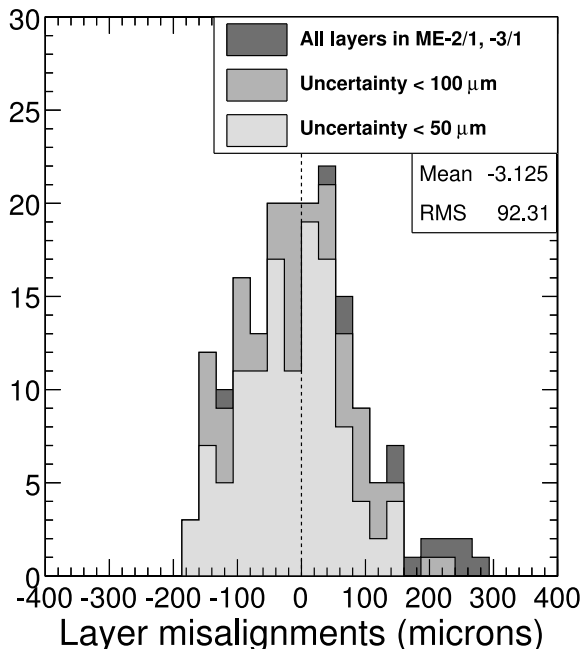


Figure 30: Layer alignment results in ME-2/1 and -3/1, excluding layers fixed by definition.

6.6 Verifying the global procedure with local alignment

In addition to providing a nearly-complete alignment of the muon endcaps before first collisions, the CSC Overlaps procedure will diagnose the global alignment procedure. Once collisions muons have been collected in sufficient quantity, we will attempt to align the CSCs with global tracks, then check it against the locally-measured result. If the global alignment is correct, it should reproduce the local results, though possibly with lower precision and an overall ring displacement, unobserved by the local measurement.

As previously stated, local track-fitting does not suffer from potential propagation errors, and it is completely independent of any tracker misalignments. Overlaps tracks are a minority, so they can be explicitly excluded from the global alignment procedure for perfect independence. It's also worth noting that the direction in which the CSC Overlaps procedure correlates results, among chambers in the same station, is orthogonal to the way global alignment correlates results, among equal-numbered chambers in different stations. If the global procedure independently aligns chamber i and $i + 1$ to the correct relative values, that would be a strong confirmation.

The local alignment procedure provides a link between the global procedure and photogrammetry. Photogrammetry must be performed when the magnetic field is off and disks are unbent. The global alignment procedure must be performed with the magnetic field on to apply an essential p_T cut; modifications of the global procedure without a p_T cut determined by track curvature would make the comparison less meaningful. Comparing the two is complicated by the fact that the geometry changes when the field is turned on. Local

alignment procedures, however, can be performed with or without the magnetic field, because local tracks are approximately linear in either case. We have verified that the CSC Overlaps procedure reproduces photogrammetry with no field; what remains is to verify that the global alignment procedure reproduces the CSC Overlaps.

If there is a discrepancy between local and global alignment results, the similarities between the methods suggest follow-up studies. For instance, some tracks pass through both the tracker and the overlap region of a CSC. We could fit the same track both ways and look for discrepancies on a track-by-track basis. Studies such as these would not be possible to diagnose differences between track-based alignment and photogrammetry or a hardware-based alignment.

7 Alignment outlook for 2009–2010

This is where I will review the steps toward alignment in 2009 and present track resolutions from the 50 and 200 pb⁻¹ scenarios derived from the “MC Results” section. It will be a schedule of future tasks, a summary of the paper, and a reference for what this alignment means for physics (Fig 31).

References

- [1] TDR
- [2] internal DT reference
- [3] <https://twiki.cern.ch/twiki/bin/view/CMS/CMSConventions>
- [4] tracker HIP
- [5] photogrammetry
- [6] MINUIT
- [7] <https://twiki.cern.ch/twiki/bin/view/CMS/SWGuideMuonGeometryConversion>

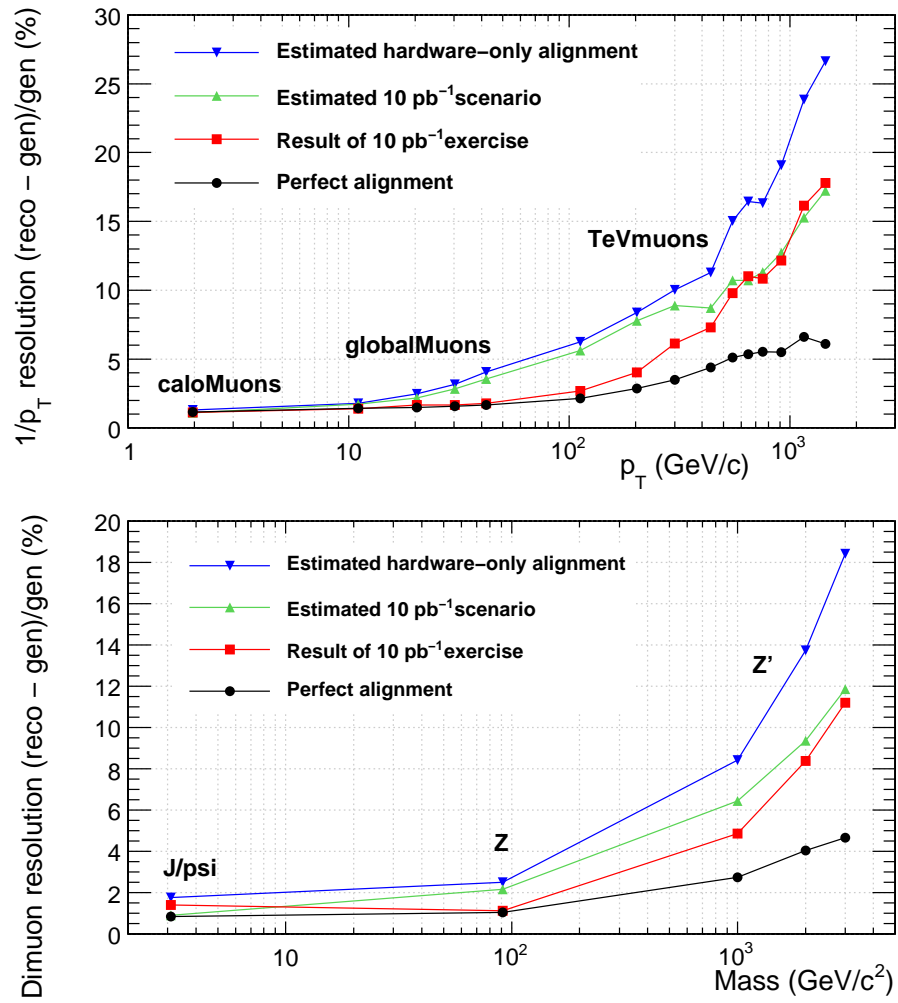


Figure 31: PLACEHOLDER! Track and mass resolutions with 2008-STARTUP, 50, 200 pb⁻¹, and ideal scenarios from the new MC studies.